

EXPERIMENTAL SUMMARY

Andreas Høecker

CERN, CH-1211 Geneva 23, Switzerland



Summary of the experimental results presented at the 51st edition of the Moriond Electroweak and Unified Theories conference held in March 2016 at La Thuile, Italy.

1 Introduction

The 51st Moriond Electroweak and Unified Theories conference featured, as is tradition, a vibrant snapshot of newest results and trends in the fields of neutrino physics, astrophysics and cosmology, gravitational waves (!), dark matter and collider physics (it became the promised LHC feast). There were 53 beautifully prepared talks in addition to young scientist presentations reporting a wealth of new experimental results that demonstrated once again that our field lives in data-driven times. The following is an attempt for a (necessarily incomplete) summary of the results presented.

2 Neutrino Physics

The year 2015 has seen yet another Nobel Prize for particle physics, and another one for neutrino oscillation. It was awarded jointly to Takaaki Kajita and Arthur B. McDonald from the Super-Kamiokande and Sudbury Neutrino Observatory experiments, respectively,¹ “for the discovery of neutrino oscillations, which shows that neutrinos have mass”.

Since these dramatic developments at the turn of the millennium neutrino physics has come a long way. Beyond the established facts that neutrinos are massive fermions with three active flavours and mass eigenstates that are mixed flavour states, there are, however, yet critical questions.

- What is the nature of the neutrinos, are they Majorana fermions?

- While the absolute mass splitting, Δm_{ij}^2 , and mixing angles, θ_{12} , θ_{13} , θ_{23} , are known to about 3% and 3–7%, respectively, the mass hierarchy is not. By convention *normal hierarchy* is dubbed the case where $m_3^2 \gg m_2^2 > m_1^2$ and *inverted hierarchy* stands for $m_2^2 > m_1^2 \gg m_3^2$.
- *CP* violation in the neutrino sector, described by the phase δ_{CP} in the Pontecorvo-Maki-Nakagawa-Sakata (PMNS) neutrino mixing matrix, is so far unknown.
- Are there sterile neutrinos, i.e., neutrinos that interact only with gravity but are singlets with respect to the Standard Model interactions? Are there heavy additional right-handed neutrinos? If so, are they in reach of current experiments?
- And also, neutrino cross section and flux measurements and their theoretical predictions need to be improved.

The experimental tools to get handles on these questions are neutrino oscillation measurements (short and long baseline), single beta decay measurements, searches for neutrinoless double-beta decay, and cosmology.^a Neutrinos also serve as messengers in astronomy, Sun and Geo science, as well as for phenomena such as grand unification, lepto/baryogenesis and physics beyond the Standard Model. Given the amount and importance of the open questions, and the variety of the available tools, neutrino physics benefits from an exciting experimental programme.

2.1 Results from short-baseline neutrino experiments

Low-energy scattering interactions of electron neutrinos or antineutrinos with matter has been a longstanding source of uncertainty. Apart from the controversial LSND result,⁴ there was the 2013 electron-neutrino appearance measurement by the MiniBooNE experiment at Fermilab that revealed in both neutrino and antineutrino beam modes⁵ an excess of events in the 0.2–0.4 GeV electron-neutrino energy range over the expectation, which is composed of (in order of importance) π^0 misidentification, $\Delta \rightarrow N\gamma$, muon and kaon decays, and other background sources. The excess appears electron-like in MiniBooNE’s Cherenkov detector, which cannot separate the signal from photon backgrounds. It is therefore important to have precise alternative low-energy cross-section measurements. This is the task of the new MicroBooNE experiment at Fermilab that is installed ~ 500 m from the Booster Neutrino Beamline (BNB) (anti)muon-neutrino beam, and is dedicated to low-energy neutrino cross sections measurements of (anti)electron appearance.³ Because the LAr-TPC tracking-calorimeter technique is similar to that of the future large-scale DUNE (LBNF) neutrino experiment, featuring a kiloton of such a detector, MicroBooNE also represents a pilot project of that experiment. In a LAr-TPC a charged particle interacts with the liquid argon, wire planes detect drifting ionisation electrons (\rightarrow tracks), photomultipliers detect scintillation light, and dE/dx is used to separate between electrons and photons. Very first and promising commissioning results from October 2015 with muon-neutrino beam scattering reactions in MicroBooNE’s 170 ton LAr-TPC were presented at this conference.

The MINERvA experiment at Fermilab performs detailed studies of neutrino interactions in varying nuclear targets (C, Pb, Fe, H₂O) with the aim to help improve the modelling of these processes.⁶ For example, electron-neutrino quasi-elastic charged-current (CCQE) scattering is an oscillation signal, but only little low-energy cross-section data are available. Can the $\nu_\mu \rightarrow \nu_e$ cross-section measurements be universally trusted? MINERvA sits on-axis at a short baseline along the NuMI (Neutrinos at the Main Injector) muon-neutrino beam, approximately 1 km after the NuMI target. During the low-energy NuMI running the beam peaks at 3.1 GeV muon-neutrino energy. The MINERvA detector features charged particle as well as electromagnetic

^aThe combination of Lyman- α , CMB and BAO data allows to set the upper limit² $\sum m_\mu < 0.12$ eV.

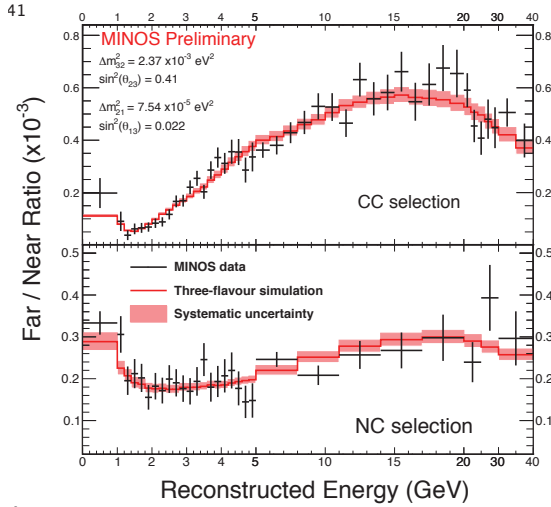


Figure 1 – Ratios of the far-to-near detector counts versus the reconstructed neutrino energy for the charged-current (top panel) and neutral-current (bottom panel) selected events. The red band shows the prediction of the three-neutrino-flavour model with systematic uncertainty.

and hadronic energy reconstruction, particle identification, and it uses the MINOS near detector as muon spectrometer. The exclusive measurement of flux-integrated differential cross sections for ν_e and $\bar{\nu}_e$ CCQE-like interactions ($\nu_e n \rightarrow e^- p$ and $\bar{\nu}_e p \rightarrow e^+ n$) on nucleons in a hydrocarbon target by MINERvA and comparison with modelling expectations (from the neutrino event generator GENIE) exhibits sufficiently good modelling for the current needs of the neutrino oscillation experiments.⁷ A nearly three times larger dataset has been already collected. The next step in the experimental programme consists of measurements at higher neutrino beam energy.

2.2 Results from long-baseline neutrino experiments

There are three present programmes for long-baseline neutrino experiments at Fermilab (MINOS, NOvA), in Japan (Tokai-to-Kamioka — T2K) and at CERN (OPERA). Long-baseline experiments measure muon-neutrino disappearance and $\nu_\mu \rightarrow \nu_e$ appearance, as well as their anti-processes. Their probabilities depend on $\sin^2(2\theta_{13})$, which is well measured and large, on $\sin^2(2\theta_{23})$, Δm_{32}^2 , and δ_{CP} , and on the sign of Δm_{31}^2 that sets the mass hierarchy. All these properties can be experimentally addressed.

The MINOS experiment consists of a 24 ton near detector (ND), placed about 1 km from the NuMI beam target, and a 4.2 kiloton far detector (FD) installed 735 km away from the target and 705 m underground in the Soudan mine. Both near and far detectors are magnetised tracking/sampling calorimeters, segmented into planes of steel and scintillator strips. The detectors are designed to have equivalent functionality so that systematic uncertainties in the neutrino flux modelling and interaction cross sections cancel in the ratio. MINOS released in May 2014 a combined analysis of its muon-neutrino disappearance and $\nu_\mu \rightarrow \nu_e$ appearance data with results for Δm_{32}^2 and $\sin^2\theta_{23}$. At this conference MINOS reported on a search for sterile neutrino using the muon-neutrino beam.^{8,9} Presence of a fourth (sterile) neutrino (ν_{sterile}) requires to introduce six new parameters to the PMNS matrix (three plus one flavour model). For simplicity the

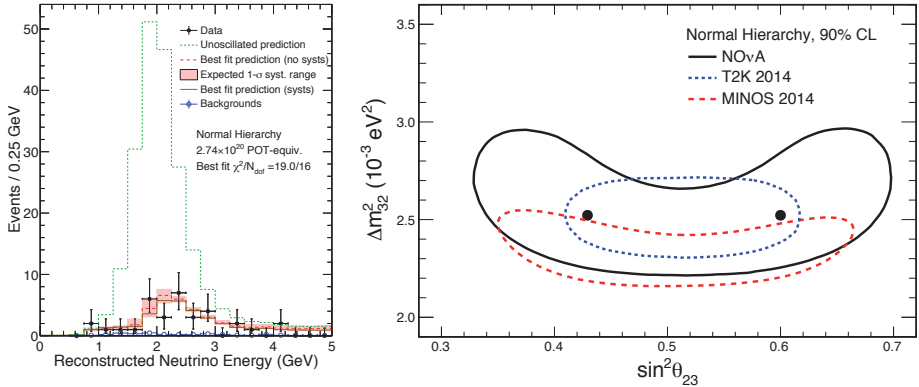


Figure 2 – The left panel shows the reconstructed neutrino energy distribution in the NOvA far detector. The green dotted line indicates the expected distribution without ν_μ disappearance. The data are significantly lower and well fitted with an oscillating signal. The oscillation parameter constraints obtained from these data are shown in the right panel, compared to other experiments.

additional CP phases and θ_{14} are set to zero, and the fit to data determines simultaneously the parameters Δm_{32}^2 , Δm_{41}^2 , θ_{23} , θ_{24} , θ_{34} . Because $\nu_{\text{active}}-\nu_{\text{sterile}}$ mixing may affect the ND reference measurement, which conventionally is assumed not to be affected by neutrino oscillation, a combined fit of the FD/ND ratio is performed. That fit shows agreement with the three-flavour model (c.f. Fig. 1) allowing to derive limits on the additional four-flavour sterile neutrino parameters that improve over constraints from other experiments.

The new NOvA long-baseline neutrino experiment at Fermilab consists of a 14 kiloton FD, 810 km away from target, installed on surface, and a 0.3 kiloton ND, both using fine-grained tracking-calorimeter technology.¹⁰ NOvA is placed 0.8° off-axis from the NuMI beam so that the muon-neutrino beam^b energy spread is reduced with peak at about 2 GeV close to the maximum muon-neutrino disappearance and electron-neutrino appearance probabilities. NOvA allows to identify electron-neutrino reactions. First NOvA results are based on data taken between November 2014 and June 2015 with a low-intensity (< 500 kW) beam. Electron-neutrino cross-section measurements found somewhat larger values than T2K and Gargamelle, which is input to the GENIE modelling. An initial measurement of muon-neutrino disappearance¹¹ provided a first constraint on Δm_{32}^2 and $\sin^2\theta_{23}$, both in agreement with earlier results from MINOS and T2K, but not yet reaching their precision (see Fig. 2). A first $\nu_\mu \rightarrow \nu_e$ appearance measurement¹² resulted in 6/11 events observed with the use of two different analysis methods (LID/LEM) in the FD for about one expected background event (estimate based on ND measurements). This corresponds to an excess of $3.3/5.3\sigma$, respectively, with the LEM result being less compatible with the inverted hierarchy. NOvA results with a twice larger dataset are forthcoming. Data with increased beam power (700 kW) are expected to be taken in 2016.

The Japan-based experiment T2K¹³ has a 295 km long baseline, using as FD Super-Kamiokande a Cherenkov detector with pure water as active material, and the NDs INGRID (on axis) and ND280 (off-axis), featuring different target materials, though currently only carbon was deployed. T2K is placed 2.5° off beam axis providing a narrow neutrino energy at a peak value of about 0.6 GeV. A combined ν_μ disappearance and ν_e appearance analysis using T2K's 2010–2013 data provided the world's best measurements of Δm_{32}^2 and $\sin^2\theta_{23}$. During the 2014/2015 runs

^bWith magnetic horns focusing on positive mesons the NuMI beam is composed of 97.6% ν_μ , 1.7% $\bar{\nu}_\mu$, 0.7% ν_e and $\bar{\nu}_e$ for neutrino energies between 1 and 3 GeV.

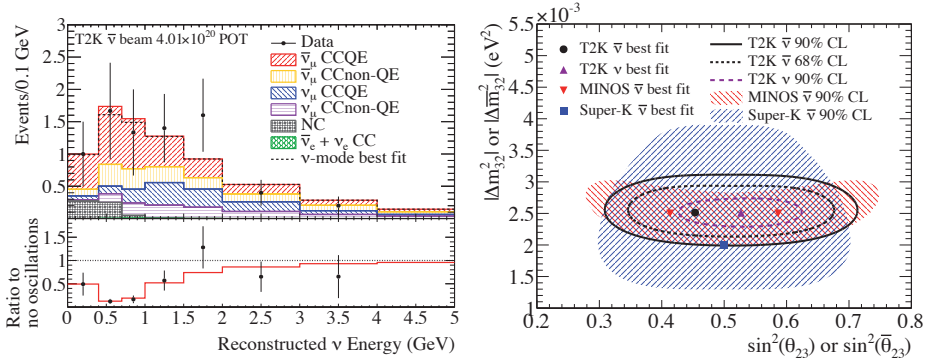


Figure 3 – Anti-muon-neutrino disappearance signal measured by T2K in a (dominantly) anti-muon-neutrino beam. The left panel shows the 34 data events seen in the far detector compared to the best fit prediction. The right panel shows the extracted (anti-)oscillation parameters.

T2K operated in $\bar{\nu}_\mu$ beam mode with 390 kW beam power collecting a total of $11 \cdot 10^{20}$ protons-on-target (POT). The antineutrino beam being less pure, the larger wrong-sign background must be measured in the ND giving about 10% flux and cross section systematic uncertainty. This is improved with the use of a combined fit of the neutrino flux model together with external and ND280 data as input to the oscillation fit. Such a complex extraction is required because FD and ND use different target and measurement technologies. The measurement of $\bar{\nu}_\mu$ disappearance yielded a significant deficit with only 34 muon events (c.f. Fig. 3), hence a clear sign of oscillation, while that of $\bar{\nu}_e$ appearance with 3 electron events seen is not yet significant.¹⁵

The European long-baseline programme concentrated on the search for tau-neutrino appearance from the conventional muon-neutrino beam sent from CERN to the 732 km away OPERA detector in the Italian Gran-Sasso Laboratory (CNGS). A breakthrough for this experiment was achieved with the July 2015 observation of a fifth tau-neutrino candidate exceeding the threshold of 5σ for the $\nu_\mu \rightarrow \nu_\tau$ appearance observation.¹⁶ In OPERA charged-current neutrino interactions ($(\nu_\mu \rightarrow) \nu_\tau + N \rightarrow \tau^- (\rightarrow e, \mu, h) + X$) are recorded in detectors (bricks) of lead and emulsion film with sub-micron resolution. The total target size consists of 150 thousand bricks. OPERA features additional target trackers and muon spectrometers. Tau-neutrino candidates are identified by tracks with a large impact parameter from the tau decay and no muon from the primary interaction vertex. Data between 2008 and 2012 were used, corresponding to $18 \cdot 10^{19}$ POT giving 20 thousand neutrino interactions in the detector of which 6.7 thousand were fully analysed.¹⁴ The five identified tau candidates consist of three one-prong and one three-prong hadronic decays, and one muon decay. The pure muon decay candidate has a very small background expectation of 0.004 ± 0.001 events. The overall background expectation is estimated to be 0.25 ± 0.05 events, the expected signal 2.64 ± 0.53 events, which is compatible with the observed five events. The signal significance is 5.1σ hence establishing the observation of tau-neutrino appearance. OPERA also set limits on sterile neutrinos. The OPERA physics programme has now ended.

2.3 Results from (short-baseline) reactor experiments

New neutrino measurements from experiments placed close to nuclear reactors in China (Daya Bay) and France (Double Chooz) were reported. Nuclear reactors represent powerful $\bar{\nu}_e$ sources from beta-decay of the nuclear fission products. Detectors installed in their $\mathcal{O}(\text{km})$ vicinity can

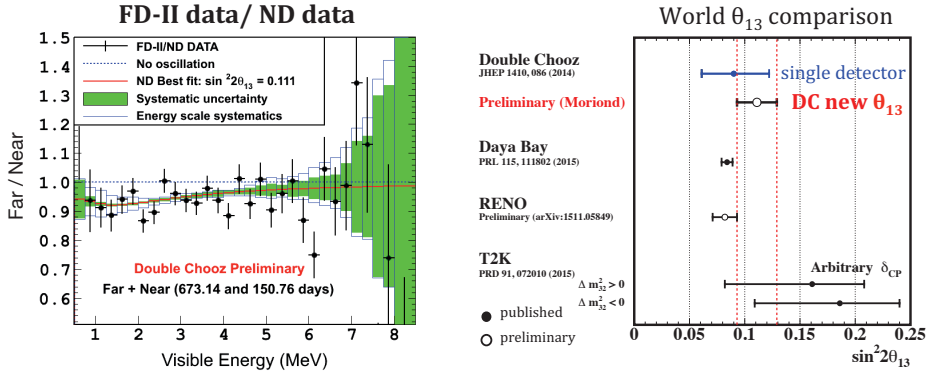


Figure 4 – **Left:** ratio of far (FD-II) to near detector yields versus visible energy measured by Double Chooz. Overlaid is the best fit result. The no-oscillation hypothesis is clearly excluded. **Right:** comparison of $\sin^2(2\theta_{13})$ measurements.²⁰

measure the mixing angle θ_{13} from the $\bar{\nu}_e$ survival probability that is dominated by the Δm_{32}^2 term.

The Daya Bay detector has completed its full assembly. It consists of two near experimental areas (effective baselines 512 m and 561 m from the 17.4 GW thermal power reactor near Hong Kong) and one far area (1.6 km). The detection of $\bar{\nu}_e$ occurs through the inverse beta decay (IBD) reaction $\bar{\nu}_e + p \rightarrow e^+ + n$ in gadolinium (Gd) doped liquid scintillators. The prompt e^+ annihilation photon and delayed 8 MeV photons from the neutron capture are measured. The $\bar{\nu}_e$ flux uncertainty is largely eliminated by simultaneous measurements at the three different detector sites. Daya Bay already provided the world’s most precise measurement $\sin^2(2\theta_{13}) = 0.084 \pm 0.005$ using data taken between October 2012 and November 2013 and using two third of the total of eight antineutrino detectors.¹⁷ The new analysis presented at this conference used neutrons captured by hydrogen (instead of Gd) providing an additional θ_{13} measurement as the data sample is largely independent and the systematic uncertainties different. It found^{18,19} $\sin^2(2\theta_{13}) = 0.071 \pm 0.011$ (nH) and, when averaged with the Gd result, $\sin^2(2\theta_{13}) = 0.082 \pm 0.004$ (nGd & nH).

The Double Chooz collaboration presented their brand new oscillation measurement at this conference.²⁰ Double Chooz installed at the Chooz nuclear power plant in France (close to the Belgium border) with two operating units (B1 and B2) has terminated its multi-detector setup with a near detector (0.4 km from the nuclear cores, available since 2015) and a far detector (1.1 km, available since 2011). The nearly iso-flux setup of the detectors reduces the flux uncertainty to less than 0.1%. The uncorrelated detection systematic uncertainty is lower than 0.3%. Double Chooz performs a combined parameter fit to the FD-I, FD-II and ND data (c.f. left panel of Fig. 4 for the ratio FD-II/ND), including also reactor-off data to constrain backgrounds. The preliminary result $\sin^2(2\theta_{13}) = 0.118 \pm 0.018$ has a significance of 5.8σ and is in agreement with previous measurements. The right panel in Fig. 4 shows a comparison of $\sin^2(2\theta_{13})$ measurements (not including the latest Daya Bay combination).

Reactor flux anomalies

Daya Bay reports a recent $\bar{\nu}_e$ flux measurement²¹ using 340 thousand near-detector IBD candidates, with better than 1% energy calibration, and comparison with model predictions: an overall deficit in data of about 2σ is found and a significant local deviation at around 5 MeV an-

tineutrino energy. While an overall deficit may seem like disappearance to a sterile neutrino, the local deviation does not. These findings are consistent with the reactor neutrino anomaly picture emerging from earlier short baseline measurements (Daya Bay, Reno, Double Chooz) that found a ratio of measured to expected $\bar{\nu}_e$ flux of about 0.94. It was reported at this conference²² that much caution is needed when interpreting these results as systematic uncertainties in the flux modelling may in total cover the observed deficit. The 5 MeV bump may be due to several fission daughter isotopes (e.g., uranium 238 or plutonium). Therefore one cannot currently consider seriously new physics claims based on absolute reactor flux comparisons. There is ample literature about the reactor flux anomaly.²³

Approximately ten very-short-baseline experiments are currently in their construction or planning phases with the aim to provide additional absolute flux measurements. Among these is the SoLid experiment, a 3 ton highly segmented plastic scintillation detector coated with Lithium-6, designed to measure flux and energy of $\bar{\nu}_e$ at distances between 6–10 m from the compact BR2 test reactor with a highly-enriched uranium core in Mol (Belgium). The main experimental challenges are the suppression of background in the proximity of the reactor (requiring a good separation of captured-neutrons versus e/γ) and the precise location of the IBD products. To achieve this, not only the time difference but also spatial information is used to reconstruct IBD events. The goal of SoLid is to run the experiment for three years to resolve the reactor neutrino anomaly without relying on theoretical modelling.²⁴

2.4 Neutrinos from the Sun

The Borexino collaboration reported new measurements²⁵ after their 2014 breakthrough evidence for detection of the Sun’s primary proton–proton fusion neutrinos, found within 10% precision to have a yield consistent with the Sun’s photon luminosity.²⁶ Borexino was initially designed for studying the 0.86 MeV Be-7 solar electron-neutrinos via ν_e - e scattering and electron recoil measurements (also IBD). The experiment consists of a 270 ton liquid scintillator, surrounded by 890 ton buffer fluid. It is installed in a 9.5 m diameter nylon vessel, 1.3 km underground at the Gran Sasso Laboratory (LGNS). The extremely high radiopurity of Borexino allows for a 250 keV neutrino energy threshold. Since that seminal 2014 result Borexino focused on the highly challenging detection (proof) of the catalytic CNO cycle in the Sun, a complex chain of CNCNONC transitions involving different C, N, O isotopes and believed to be the dominant energy source in stars more massive than the Sun. Borexino also performed tests of electron charge conservation through the search for $e \rightarrow \gamma\nu, \nu\nu\nu$ decays achieving the world’s best electron lifetime sensitivity $\tau_e > 6.6 \cdot 10^{28}$ years; and the 5.9σ observation of geological $\bar{\nu}_e$ for which the largest background stems from nuclear reactors.^{28,27}

2.5 Neutrino astronomy

Cosmic rays have been measured over eleven orders of magnitude in energy, but their highest-energy sources are not well known yet. Several favourable conditions make neutrinos from outer space to excellent astronomical probes for the study of cosmic rays. Neutrinos are not deflected by astrophysical foreground and therefore point back to their sources. Moreover, owing to their characteristic scattering signatures, the flavour of neutrinos can be reconstructed in a large detector providing information about their origin.

IceCube²⁹ is a spectacular experiment buried between 1.5–2.5 km deep in South Pole ice. It has an active volume of about 1 km^3 distributed among 86 strings. IceCube measures Cherenkov light “track” and “cascade” (shower) signatures that are characteristic charged-current interactions in ice of muon-neutrinos and electron-neutrinos, respectively. A so-called “double-bang”

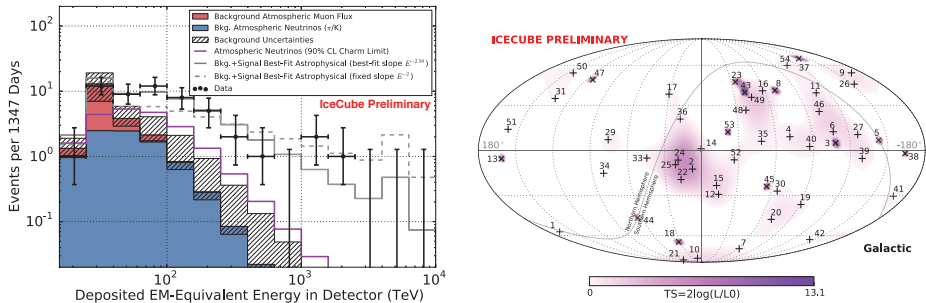


Figure 5 – **Left**: inclusive neutrino energy spectrum measured by IceCube after four years of data taking. Also shown are the estimated atmospheric backgrounds. **Right**: arrival directions of the neutrino events in galactic coordinates. Shower-like events are marked with '+' and those containing tracks with 'x'. Colours show the test statistics value for point-source clustering at each location. No significant clustering was found. Both figures are taken from Ref.³⁰.

event would be signature for a tau-neutrino in which a produced tau lepton of PeV energy penetrates 50 m ice in average before it decays leaving a hadronic or electromagnetic shower. IceCube detected interactions from about 100 thousand neutrinos with larger than 200 GeV energy per year, among which a few dozens are of astrophysical origin, and the majority stems from atmospheric muon and muon-neutrino background.

IceCube measured the inclusive neutrino energy spectrum above 60 TeV during four years of data taking (see left panel of Fig. 5). A total of 53 good events were found up to around 2 PeV energy with a significance of 6.5σ for a signal of astrophysical neutrinos. The energy spectrum was found to be somewhat harder than expected indicating that the canonical E^{-2} model may be insufficient to describe the data.³⁰ IceCube also sees a 5.9σ excess of up-going muon-neutrinos (charged current only) in the 0.2–8.3 PeV energy regime over atmospheric background normalised to data at 100 TeV neutrino energy. A possible pattern in the spectral index versus the neutrino energy cannot be excluded. The measured arrival directions of the observed astrophysical neutrinos do not exhibit clustering that would hint to a point source (see the example in the right panel of Fig. 5).

The reconstruction of the neutrino flavour can provide information about the source of the astrophysical neutrinos. Pion decay should produce relative neutrino abundances of $\nu_e : \nu_\mu : \nu_\tau = 1 : 1 : 1$ on earth, if muons are suppressed due to, e.g., large magnetic fields in space the relative abundances would be $1 : 1.8 : 1.8$, and if the neutrinos originate from neutron decay one would expect to see a pattern of $2.5 : 1 : 1$. The current IceCube data are consistent with the first two but exclude the third pattern. No hint for tau neutrinos was found yet but is expected to occur in the accumulated data sample.

IceCube also belongs to the elite of experiments who have observed neutrino oscillation through muon-neutrino disappearance. The measurement of Δm_{32}^2 and θ_{23} is consistent with that from other experiments. IceCube also searched for sterile neutrinos, heavy dark matter annihilation, and solar flares.³¹ A next generation experiment, IceCube-Gen2, covering an active area of about 10 km^3 , is currently in its R&D phase.

2.6 Of which quantum nature are neutrinos?

The yet unrevealed Majorana or Dirac nature of neutrinos can be addressed experimentally by detecting neutrinoless double beta ($0\nu\beta\beta$) decay (c.f. diagrams in Fig. 6), which would indicate

that there is a non-zero Majorana mass term as Dirac neutrino masses do not mix neutrinos and antineutrinos.^c Through the relation $\Gamma_{0\nu\beta\beta} \propto |M_{0\nu\beta\beta}|^2 \langle m_{\beta\beta} \rangle^2$ and theory input for the nuclear matrix element one can via the measurement of or bound on $\Gamma_{0\nu\beta\beta}$ infer information on the neutrino mass and hierarchy. Experiments searching for $0\nu\beta\beta$ decay require large mass, high isotopic abundance, good energy resolution, high efficiency and low background. Results from the EXO-200 and CUORE-0 experiments were reported at this conference.^{36,33}

EXO-200 is a detector that uses an enriched (81%) liquid-xenon TPC ($^{136}\text{Xe} \rightarrow ^{136}\text{Ba} + 2e^-$) and is installed in a nuclear waste isolation plant in New Mexico, US. EXO-200 presented in 2014 a result using data corresponding to 100 kg · years of ^{136}Xe exposure³⁴ with no evidence for $0\nu\beta\beta$ decay giving a half-life lower limit of $1.1 \cdot 10^{25}$ years at 90% CL. This corresponds to $\langle m_{\beta\beta} \rangle < (190-470)$ meV, where the range is due to different theoretical assumptions on the nuclear matrix element. A recent analysis^{35,36} reported at this conference searched for the $2\nu\beta\beta$ decay of ^{136}Xe to the 0_1^+ excited state of ^{136}Ba , which de-excites via two photons. No significant signal was found in that search.

The LGNS based experiment CUORE-0, a prototype of the full CUORE experiment, employs a bolometric technique using an array of tellurium dioxide crystals ($^{130}\text{Te} \rightarrow ^{130}\text{Xe} + 2e^-$) cooled down to remarkable 10 mK. The bolometer benefits from excellent energy resolution but no particle identification capability. A first CUORE-0 measurement^{32,33} using a ^{130}Te exposure of 9.8 kg · years revealed no signal at the expected $Q_{\beta\beta}$ value of 2528 keV, giving, when combined with a previous Cuoricino result, the 90% CL limit $\langle m_{\beta\beta} \rangle < (270-760)$ meV, where again the range reflects the matrix element uncertainty.

3 Proton decay — GUT messengers

It is not possible to reach energies in the laboratory that would allow to directly study the physics at the expected grand unification scale. Even Enrico Fermi’s “Globatron” (that was to be built in 1994) would with current LHC magnet technology “only” reach insufficient 20 PeV proton–proton centre-of-mass energy. Proton decay is among the greatest mysteries in elementary particle physics. It is required for baryogenesis and predicted by grand unified theories (GUT). Its discovery could therefore provide a probe of GUT scale physics.

All current limits are dominated by searches at the Super-Kamiokande (SK) experiment.^d New results from SK combining all SK I–IV data (1996–now) were presented at this conference.³⁸ No significant excess was found leading to the following strong limits: $\tau(p \rightarrow e^+\pi^0) > 1.7 \cdot 10^{34}$ years (no events seen in the signal regions R1/2, for 0.07/0.54 background events expected), $\tau(p \rightarrow \mu^+\pi^0) > 7.8 \cdot 10^{33}$ years (less sensitive because the μ^+ is detected through its decay to e^+ , 0/2 events seen in R1/2, for 0.05/0.82 background events expected), $\tau(p \rightarrow K^+\nu) > 6.6 \cdot 10^{33}$ years (the K^+ being below Cherenkov threshold is detected through its decay, no events seen in signal regions SB/C, for 0.39/0.56 background events expected), The SK collaboration also looked for more exotic phenomena.

^cMajorana masses cannot originate from a Yukawa coupling to the Standard Model Brout-Englert-Higgs (BEH) field and thus would make neutrinos very different from the other known fermions.

^dWe recall that “KamiokaNDE” stands for “Kamioka Nucleon Decay Experiment”.

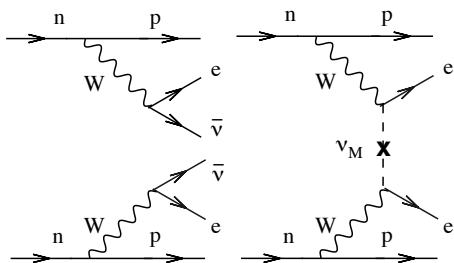


Figure 6 – Representative Feynman diagrams for two-neutrino double beta decay (left) and neutrinoless double beta decay (right). Figures taken from Ref.³⁷.

An order of magnitude gain in sensitivity on $\tau(p \rightarrow e^+\pi^0)$ is expected from the Hyper-Kamiokande project which has 25 times the size of SK (SK holds 50 kiloton of pure water) and has an expected begin of construction in 2018.

4 Direct dark matter searches

Direct dark matter experiments search for elastic collisions of a weakly interacting massive particle (WIMP) from the galactic halo with a target nucleus at rest in the laboratory. With an assumed WIMP average speed of about 220 km per second the collision is expected to lead to a measurable nuclear recoil of about 20 keV. The effective scattering Lagrangian may have scalar (spin-independent, $SI \propto A^2$, where A is the atomic number of the target nucleus) or axial-vector (spin-dependent, $SD \propto$ nuclear spin, no coherent amplification) terms. The dominant background stems from electrons recoiling after X-ray or γ -ray interactions. Direct dark matter experiments have similar challenges to overcome as neutrino experiments. They must be deep underground, have excellent radiopurity, must be shielded around the active detector volume and they require redundant signal detection technologies.

The CDMSlite experiment (CDMSlite stands for CDMS low ionisation threshold experiment) is located at the US Soudan Underground Laboratory. CDMS looks for keV-scale recoils from elastic scattering of WIMPs off target nuclei. It uses up to 19 Ge and 11 Si detectors. Ionisation charges and phonons (heat) are measured and used to discriminate electron from nuclear recoils. CDMSlite operates one Ge detector at increased bias voltage to amplify the phonon signal and gain sensitivity to lower WIMP masses. Two runs were taken with the second benefiting from reduced acoustic noise (hence a lower threshold) and longer exposure. The newly^{39,40} excluded parameter space for SI WIMP–nucleon interaction extends to WIMP masses down to 1.6–5.5 GeV and cross sections between 10^{-37} – 10^{-41} cm^2 . With this measurement the SuperCDMS programme has ended. It will be followed up by SuperCDMS at SNOLAB (2.1 km deep underground).

The CRESST-II experiment at the LNGS has further improved its sensitivity to even lower mass WIMPs. Energy threshold is key for this search. CRESST-II uses cryogenic calcium tungstate (CaWO_4) crystals to measure scintillation light and phonons to separate electron from neutron recoils. Transition edge sensors (TES, about 15 mK) and a squid system measure, amplify and read out the signal, allowing sub-keV energy thresholds and a high-precision energy reconstruction. Combined with the light target nuclei, CRESST-II has the potential to probe < 1 GeV dark matter particles. At 0.5 GeV a limit of about 10^{-36} cm^2 was obtained.^{41,42} Systematic studies on the current data sample are still ongoing. The follow-up programme with 50–100 eV threshold starts in April 2016.

XENON100 is the second phase of the XENON dark matter experiment at LNGS running since

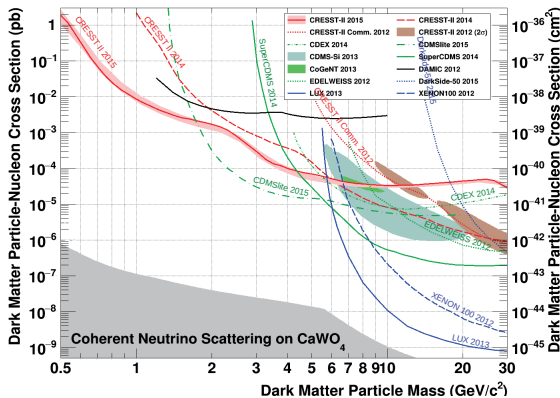


Figure 7 – Summary of low-mass WIMP–nucleon cross-section limits (in pb) versus WIMP mass.⁴²

Systematic studies on the current data sample are still ongoing. The follow-up programme with 50–100 eV threshold starts in April 2016.

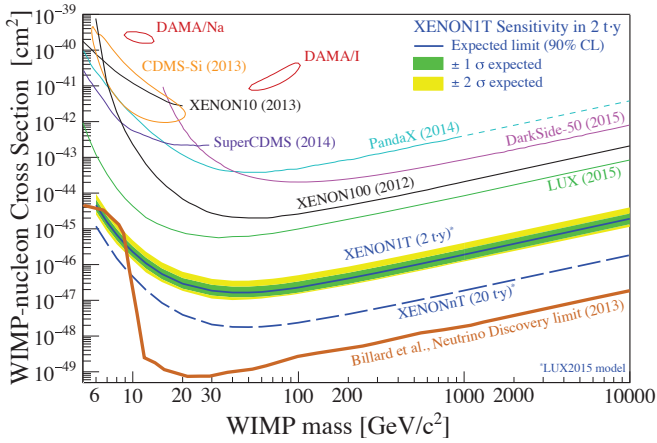


Figure 8 – Current WIMP–nucleon cross-section limits versus the WIMP mass and extrapolations (plot taken from XENONnT). The lowest bold line depicts the expected coherent ν – N scattering background.

2009.⁴⁵ It is the predecessor of the ambitious programme XENON1T. XENON100 uses a 61 (100) kg target (active veto) liquid-gas xenon (LXe) filled TPC. Liquid xenon as target material features a high density, high atomic number, sensitivity to spin-dependent interactions through approximately 50% odd isotopes, low threshold due to high ionisation and scintillation yield, low backgrounds, and a self-shielding target. The liquid xenon scintillation light is measured by photomultiplier tubes (PMT). Light from prompt scintillation (S1) and delayed ionisation (S2) allows to discriminate electron from nuclear recoil. The primary results were published⁴⁶ by XENON100 in 2012 providing powerful limits on the WIMP–nucleon interaction cross section down to about $2 \cdot 10^{-45} \text{ cm}^2$ for a WIMP mass of 50 GeV at 90% CL for SI interactions.⁴³ SD results were released in 2013 with best limits of about 10^{-38} cm^2 and $4 \cdot 10^{-40} \text{ cm}^2$ for proton and neutron cross sections, respectively.⁴⁴ A recent XENON100 analysis⁴⁷ addresses the periodic signal reported by the DAMA collaboration. XENON100 does not find significant periodicity, excluding DAMA’s phase and amplitude at 4.8σ . DAMA-like dark matter models are excluded to at least 3.6σ . The experimental follow-up programme XENON1T has its commissioning almost completed. First results are expected in the course of 2016.

Dark matter searches with the LUX experiment were also presented.⁴⁸ LUX is a liquid-Xe experiment located at the Sanford Underground Research Facility in South Dakota, US, about 1.5 km deep. LUX is very similar to XENON100 based on a dual-phase liquid Xe target. It has a larger active target and lower threshold than XENON100 (3 keV vs. 6.6 keV) and hence sensitivity to lower WIMP masses. A reanalysis of the 2013 data (95 live days, 145 kg fiducial mass) with improved calibration, event reconstruction and background modelling increases the sensitivity especially at low WIMP masses.⁴⁹ The best SI limit at WIMP masses of around 40 GeV reaches down to approximately $7 \cdot 10^{-46} \text{ cm}^2$ WIMP–nucleon cross section. LUX has also recently published SD limits using the same dataset.⁵⁰ Their follow-up programme LZ = LUX + ZEPLIN is entering CD-2 review and has a planned start for 2025.

Dark matter searches undertake and prepare a healthy experimental programme with orders of magnitude improved sensitivity. Figure 8 shows the WIMP–nucleon cross-section limits versus the WIMP mass and extrapolations. Shown by the thick red line is the irreducible coherent elastic neutrino–nucleon scattering background that is expected to be in reach with the next generation experiments.

5 Gravitational waves

The LIGO/VIRGO Collaboration, a new popstar in science, reported on February 11th, 2016 an earth-shattering measurement⁵²: a huge gravitational wave (GW) signal of a binary black hole merger detected simultaneously in the two LIGO sites (the VIRGO experiment was not operational at the time of the measurement), first noticed by its online burst detection system. This measurement is an example of scientific perseverance.⁵¹

The principle of the measurement is sketched in Fig. 9. Spin-2 GWs lengthens one arm while shortening the other and vice versa in the LIGO laser interferometer: $\Delta L(t) = \delta L_x - \delta L_y = h(t)L$. The optical signal measured is proportional to the strain $h(t)$. There are several enhancements to a basic Michelson interferometer in LIGO: test mass mirrors multiply the effect of GW on the light phase by a factor of about 300; a power recycling mirror on the input amplifies the laser light; output signal recycling broadens the bandwidth. The

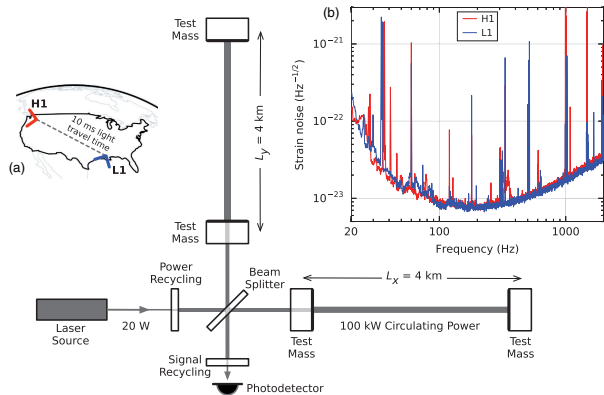


Figure 9 – Principle of the LIGO gravitational wave measurement.

test masses are isolated from seismic noise and have very low thermal noise. All relevant components of the interferometer are isolated against vibrations. The laser light passes through vacuum to reduce Rayleigh scattering of light off air molecules. A system of calibration lasers and array of environmental sensors further helps to reduce systematic uncertainties. Two (better three!) distant interferometer are needed to localise a GW and measure its polarisation.

On September 14, 2015 at 09:51 UTC (11:51 CEST), within a total of 16 days of simultaneous two-detector observational data taken by LIGO Hanford, Washington (H1) and LIGO Livingston, Louisiana (L1), the signals shown in the left panel of Fig. 10 were detected (the H1 data are shifted by 6.9 ms to allow for a better comparison). The detected GW pattern is an extremely loud event (modified signal-to-noise ratio of $\hat{\rho}_c = 23.6$). The maximum strain (10^{-21}) times the 4 km arm length gives a length deformation of $4 \cdot 10^{-18}$ m, which is about 0.5% the size of a proton. The measured spectrum can be well reproduced by GW calculations after fitting its parameters to the observation. The event, dubbed GW150914, is found to have a significance over background of more than 5.1σ . The time series shown in the figure was filtered with a 35–350 Hz bandpass filter to suppress large fluctuations outside the detectors’ most sensitive frequency band, and with band-reject filters to remove strong instrumental spectral lines.

The right panel of Fig. 10 shows a sketch of the posited black hole encounter and coalescence. Thereafter, GW150914 occurred 1.3 ± 0.5 billion years (410 Mpc) ago. Over a duration of 0.2 s, frequency and amplitude of the binary black hole system increased from 35 to 150 Hz (in about 8 cycles). To reach 75 Hz orbital frequency, the objects needed to be very close (about 350 km to each other and massive (thus black holes^e). Two black holes of initially 36 and 29 solar masses

^e*Digression.* There are gargantuan black holes in the universe. Many galaxies are expected to host supermassive black holes with more than a million times the mass of the Sun in its centre, formed during the galaxy creation process. NGC 4889, the brightest elliptical galaxy in the Coma cluster (94 Mpc \sim 300 Mly from earth), hosts a record black hole of 21 billion times M_\odot , with event horizon diameter of \sim 130 billion km (Sun: 1.4 million km).

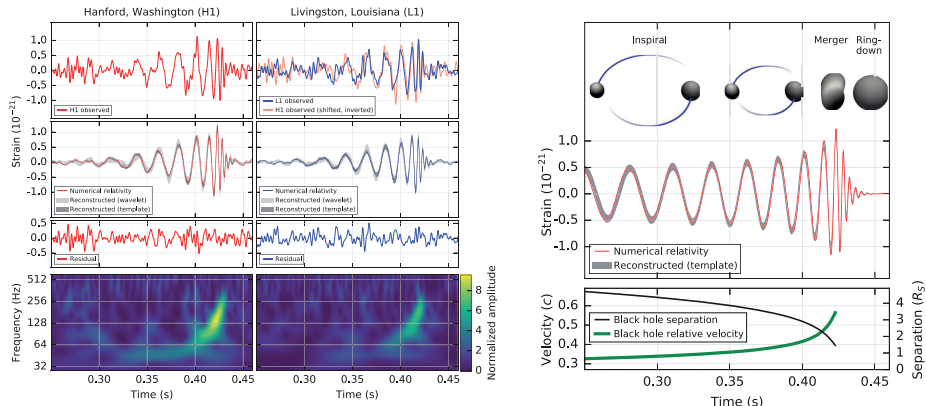


Figure 10 – **Left:** the gravitational-wave event GW150914 observed by the LIGO Hanford (H1, left column panels) and Livingston (L1, right column panels) detectors. Times are shown relative to September 14, 2015 at 09:50:45 UTC. The top panels show the measured GW strains. For a better visual comparison the H1 data are shifted in time by 6.9 ms. The panels in the second row show the GW strains projected onto each detector in the 35–350 Hz frequency band. The solid line superimpose the fit predictions based on general relativity calculations. The third row shows the residuals after subtracting the filtered numerical relativity waveform from the filtered detector time series, and the bottom panels show a time-frequency representation of the strain data, showing the signal frequency increasing over time. **Right:** estimated gravitational-wave strain amplitude from GW150914 projected onto H1. The bottom panel shows the effective black hole separation in units of Schwarzschild radii and the effective relative velocity. Figures and explanations taken from Ref.⁵².

(M_{\odot}) inspiral with about half the speed of light. The black holes merge within tens of ms; the inspiral, merging and ringdown leave a characteristic amplitude and frequency GW pattern. The total radiated GW energy amounts to $(3.0 \pm 0.5)M_{\odot}$. The direct observation of this event follows upon the indirect proof of GWs from energy loss measurements in binary pulsar systems in 1982.^{53,54}

The observation of GW150914 bundles several discoveries: it is the first direct detection of GWs, the first observation of a binary black hole merger, it shows that relatively heavy stellar-mass black holes ($> 25 M_{\odot}$) exist in nature, it is the observation of the “no-hair-conjecture” according to which any black hole can be fully characterized by only three classical observables (mass, electric charge, angular momentum), it is the most relativistic binary event ever seen ($v/c \sim 0.5$), and it leads to a new limit on the graviton mass of $< 1.2 \cdot 10^{-22}$ eV. GW150914 is likely not a unique binary black hole event. The rate is inferred to lie between 2 and 400 events per Gpc³ and year, which is at the higher end of the expectations. Adding VIRGO will improve the localisation of future GW events. New interferometers are upcoming in India and Japan. Electromagnetic and high-energy neutrino follow-up programmes are also in work (no high-energy neutrino coincidence during GW150914 was seen by ANTARES and IceCube).

Gravitational waves have joined the club for multi-messenger astronomy together with photons, cosmic rays and neutrinos. The paper reporting the observation⁵² collected more than 100 citations within a month. The LIGO/VIRGO collaboration released a number of companion papers about detector and analysis details and implications of GW150914.⁵⁵

6 Flavour Physics

Flavour physics deals with the study of flavour transitions, mixing and CP violation in all its aspects. Precision measurements and the measurement of rare, and search for forbidden processes provides sensitivity to new physics beyond the current energy frontier of direct production. By these measurements it is hoped to acquire insight into the mystery of the observed flavour structure (which is related to the BEH sector).

6.1 Tetraquarks?

Although hadron spectroscopy is not a topic traditionally discussed at this conference, it occurred that the D0 experiment at Tevatron had recently reported⁵⁶ the observation of a new state in the invariant mass spectrum of $B_s(\rightarrow J/\psi\phi)\pi^\pm$. The new state has a mass and width of 5568 MeV and 22 MeV, respectively, and a fiducial yield ratio ρ (relative to the B_s yield) between about 5 and 12%. It is compatible with a hadronic state with valence quarks of four different flavors (tetraquark) made of a diquark-antidiquark pair and quantum numbers $J^P = 0^+$. A prompt cross-check performed by the LHCb collaboration^{57,58} did not confirm the observation in a 20 times larger B_s sample. An upper limit on ρ of 1–2% depending on the fiducial region is found. Other experiments are also looking for this state. The results may depend on beam, energy and analysis differences between the experiments.

6.2 CKM Matrix

Among the central topics of flavour physics is the continuing effort to overconstrain the CKM matrix and thus test the Standard Model quark-flavour sector. LHCb has joined this effort with important contributions. A precise measurement of the CKM angle γ (through tree-level processes) together with $\sin(2\beta)$ (through mixing-induced CP violation) or $|V_{ub}|$ (through tree-level processes), fixes the apex of the CKM unitarity triangle. All other measurements probe these constraints. Among the results reported by LHCb in this area are⁵⁸: a $|V_{ub}/V_{cb}|$ measurement from $\Lambda_b \rightarrow p\mu\nu$ with 5% precision⁵⁹ that is closer to the exclusive B -factory numbers for $|V_{ub}|$ (which exhibit tension with the larger inclusive numbers), the world's best single Δm_d measurement⁶⁰ $0.5050 \pm 0.0021 \pm 0.0010 \text{ ps}^{-1}$ (the B -factories have a combined uncertainty of 0.005 ps^{-1}), a $\sin(2\beta)$ measurement⁶¹ of $0.731 \pm 0.035 \pm 0.020$ that approaches the precision of the B -factories, the world's best constraints on CP violation in $B_{(s)}^0$ mixing (a_{sl}^s, a_{sl}^d) in agreement with the Standard Model (D0 sees a 3.6σ deviation), and a search for CPT violation⁶² (difference in mass or width) in the $B_{(s)}^0$ systems together with the measurement of sidereal phase dependence of the CPT violating parameter.

LHCb has engaged into a vigorous programme⁶³ to determine the CKM angle $\gamma \sim \arg(-V_{ub}^*)$. It can be measured through interference of $b \rightarrow u$ with $b \rightarrow c$ tree transitions. The hadronic

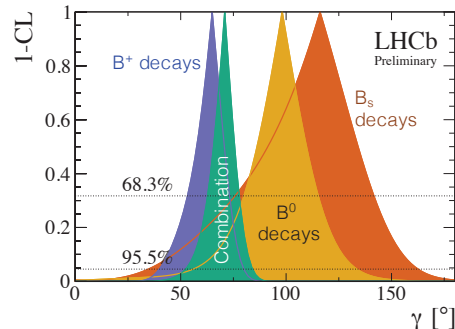


Figure 11 – Confidence level versus the CKM angle γ as obtained by LHCb⁶³ for analyses involving B^+ decays (blue), B_s decays (dark orange), B^0 decays (light orange), and their combination⁶⁹ (green).

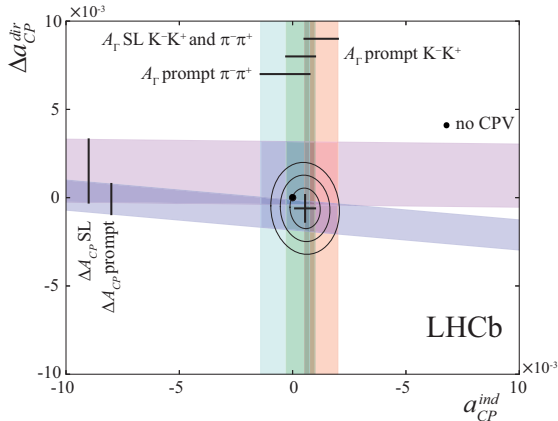


Figure 12 – CP asymmetries measured in $D^0/\bar{D}^0 \rightarrow K^+K^-/\pi^+\pi^-$ decays decomposed into direct and indirect components.⁶⁸ The measured values by LHCb are compatible with the no- CP -violation hypothesis.

parameters are the amplitude ratio r_B and the strong final-state-interaction (FSI) phase δ_B that need to be determined from data. The extraction of γ is then theoretically clean, but large statistics are needed due to the CKM suppression of some of the involved amplitudes. To fully exploit the available data LHCb uses B^\pm , B^0 , B_s , and many D decay modes requiring different techniques; also DK^* and $D_s K$ are used. Some modes show large direct CP asymmetries. It is unfortunately impossible to appropriately discuss the individual measurements in this summary, so we only show the overall results on γ in Fig. 11. The combined fit, dominated by the measurements from charged B^+ to charm decays, gives⁶⁹ $\gamma = 70.9_{-8.5}^{+7.1}$ deg, which is in agreement with the value from the CKM fit (not including the direct γ measurements) of⁶⁴ 68 ± 2 deg.

6.3 CP violation and mixing in charm decays

In the neutral charm sector the mixing probability is extremely low due to CKM suppression of order λ^{10} , making charm mixing a challenging measurement. Mixing-induced or direct CP -violation effects are also expected to be small so that for both measurements large data yields are needed. Owing to a large cross section and hadronic triggers, LHCb has collected a huge charm sample during Run-1. A new mixing analysis⁶⁶ presented at this conference used the decay $D^0 \rightarrow K^-\pi^+\pi^-\pi^+$ to determine the strong phase difference needed for the measurement of γ from $B^+ \rightarrow D^0(\rightarrow K^-\pi^+\pi^-\pi^+)K^+$ decays. It exploits the time-dependent ratio of wrong-sign ($D^0 \rightarrow K^+\pi^-\pi^+\pi^-$) to right-sign ($D^0 \rightarrow K^-\pi^+\pi^-\pi^+$) events that depends on the charm mixing coefficients, the ratio of Cabibbo-favoured and doubly Cabibbo-suppressed amplitudes, and on their interference (hence the sensitivity to the strong phase).

LHCb also presented^{65,66} a new measurement of the time-integrated CP asymmetry $\Delta A_{CP} = A_{CP}(D^0/\bar{D}^0 \rightarrow K^+K^-) - A_{CP}(D^0/\bar{D}^0 \rightarrow \pi^+\pi^-)$, where the D^0 flavour is inferred from the charge of the soft pion in the decay $D^{*\pm} \rightarrow D^0\pi^\pm$. An earlier result by LHCb⁶⁷ using 0.6 fb^{-1} of data collected during Run-1 exhibited an unexpected 3.5σ deviation from zero ($\Delta A_{CP} = 0.82 \pm 0.21 \pm 0.11$, where the first uncertainty is statistical and the second systematic). The new result⁶⁸ using the full 3.0 fb^{-1} Run-1 data sample, $\Delta A_{CP} = 0.10 \pm 0.08 \pm 0.03$, does not confirm the earlier evidence for a deviation⁶⁶ (see also Fig. 12).

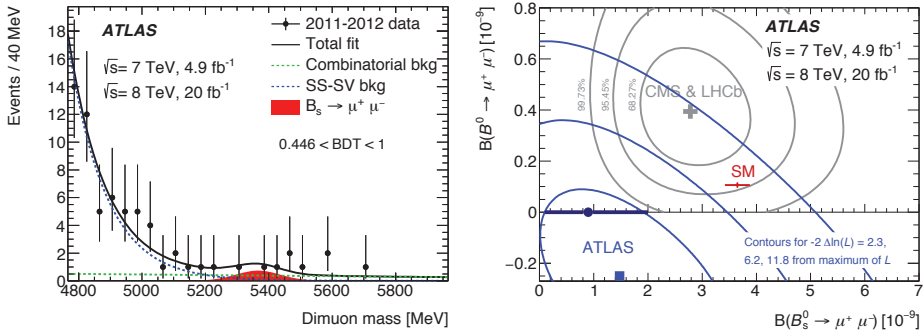


Figure 14 – **Left:** dimuon mass distribution in the most signal-like BDT bin. Data and fit results (split into signal and background components) are overlaid. **Right:** delta log-likelihood contours in the $\mathcal{B}(B \rightarrow \mu^+\mu^-)$ versus $\mathcal{B}(B_s \rightarrow \mu^+\mu^-)$ plane obtained without imposing the constraint of non-negative branching fractions. Also shown are the combined result by CMS and LHCb, the Standard Model prediction with uncertainties and the ATLAS result within the boundary of non-negative branching fractions. The figures taken from Ref.⁷⁴.

6.4 Rare B decays

The rare flavour-changing neutral current decay $B_s \rightarrow \mu^+\mu^-$ (c.f. diagrams in Fig. 13) is a prominent channel to look for new physics. It has been searched for during almost 30 years at many accelerators improving the sensitivity by five orders of magnitude before being observed by CMS and LHCb^{70,71,72} in November 2014 through a combination of their Run-1 datasets. They found $\mathcal{B}(B_s \rightarrow \mu^+\mu^-) = 2.8^{+0.7}_{-0.6} \cdot 10^{-9}$ with a significance of 6.2σ . The corresponding Standard Model prediction⁷³ $(3.7 \pm 0.2) \cdot 10^{-9}$ is in agreement with the measurement. The CKM suppressed B_d channel^f was found to be $\mathcal{B}(B \rightarrow \mu^+\mu^-) = 3.9^{+1.6}_{-1.4} \cdot 10^{-10}$ with a significance of 3.2σ . This value is larger than the prediction⁷³ $(1.1 \pm 0.1) \cdot 10^{-10}$.

At this conference, ATLAS presented their full Run-1 result for the two channels.^{74,75} The analysis proceeded similarly to that of CMS and LHCb employing a multivariate Boosted Decision Tree (BDT) to suppress hadrons faking muons giving rise to peaking backgrounds, another BDT to suppress continuum background, and a two-dimensional fit to continuum-BDT bins and the dimuon mass (unbinned) to locate the signal. The fitted event yields are normalised to $B^+ \rightarrow J/\psi K^+$ requiring as input the ratio of decay constants f_s/f_d taken from a dedicated ATLAS measurement (also requiring theoretical input). As control channels to validate the cut efficiencies and multivariate analyses serve $B^+ \rightarrow J/\psi K^+$ and $B_s \rightarrow J/\psi\phi$. The expected sensitivity of the analysis for a Standard Model branching fraction is 3.1σ . Figure 14 (left panel) shows the dimuon mass distribution in the most signal-like BDT bin. No significant signal is seen in this or the other two selected BDT bins. Constraining the two branching fractions to be non-negative in the fit gives $\mathcal{B}(B_s \rightarrow \mu^+\mu^-) = 0.9^{+1.1}_{-0.8} \cdot 10^{-9}$ with an upper limit of $3.0 \cdot 10^{-9}$ at 95% CL. The upper limit for $\mathcal{B}(B \rightarrow \mu^+\mu^-)$ is $4.2 \cdot 10^{-10}$. The compatibility with the Standard Model amounts to 2.0σ . The right panel of Fig. 14 shows the fit result in the two-dimensional branching fraction plane together with the combined CMS and LHCb result and the Standard Model prediction. Also shown is the ATLAS result within the boundary of non-negative branching fractions.

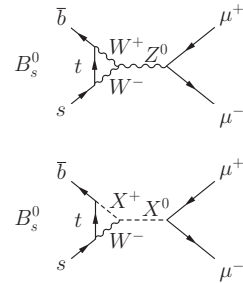


Figure 13 – Representative Feynman diagrams for Standard Model (top) and new physics (bottom) contributions to $B_s \rightarrow \mu^+\mu^-$.

^fThe d subscript in B_d is usually omitted.

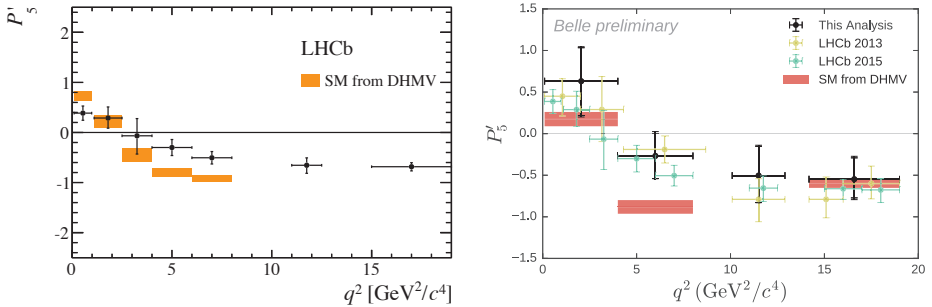


Figure 16 – The angular ratio P'_5 versus the invariant mass q^2 of the recoiling dimuon system in $B \rightarrow K^* \mu^+ \mu^-$ measured by LHCb⁷⁶ (left panel) and Belle⁷⁷ (right panel). Also shown are selected theoretical predictions.

6.5 Flavour anomalies

Several measurements in the flavour sector exhibit non-significant but interesting anomalies with respect to theory predictions. A prominent example is given by angular coefficients describing the transition $b \rightarrow s \mu^+ \mu^-$. Figure 15 shows Feynman graphs for Standard Model and putative new physics contributions. The LHCb collaboration performed an angular analysis of the decay $B \rightarrow K^* \mu^+ \mu^-$ using the full Run-1 data sample and determining eight independent CP -averaged observables.^{76,71} A convenient observable for comparison with theory is the ratio $P'_5 = S_5 / \sqrt{F_L(1 - F_L)}$ in which the form-factor uncertainty cancels. Figure 16 (left panel) shows the distribution of P'_5 versus the invariant mass q^2 of the recoiling dimuon system. The LHCb data points show a tension with the chosen theory prediction in the q^2 range between 4 and 8 GeV^2 . The Belle collaboration recently performed a measurement of that observable which is in agreement with the LHCb result but has lower statistical precision⁷⁷ (see right panel of Fig. 16).

Angular and differential branching fraction analyses were also performed for $B_s \rightarrow \phi \mu^+ \mu^-$ (also exhibiting a localised tension with the prediction) and a differential branching fraction analysis for $B^+ \rightarrow K^+ \mu^+ \mu^-$. A global fit with an effective new physics parameterisation (Wilson coefficients C_9^{NP} , C_{10}^{NP}) can reproduce the observed discrepancy pattern.⁷⁸

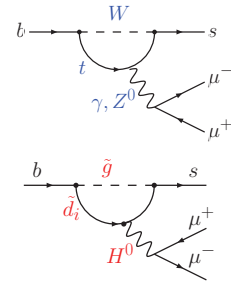


Figure 15 – Representative Feynman diagrams for Standard Model (top) and new physics (bottom) contributions to the process $b \rightarrow s \mu^+ \mu^-$.

Less plagued by hard to estimate theoretical uncertainties are lepton universality tests. Such tests were performed at the per-mil level at LEP and other $e^+ e^-$ colliders not showing any significant discrepancy with the expectation of universal lepton coupling. The B -factory experiments and LHCb have measured ratios of semileptonic B decays that have robust Standard Model predictions.^{79,80,81,71,82} Figure 17 shows the various measurements of the ratios $R_{D^{(*)}} = \mathcal{B}(B^0 \rightarrow D^{(*)} \tau \nu) / \mathcal{B}(B^0 \rightarrow D^{(*)} \ell \nu)$ (left panel) and $R_K = \mathcal{B}(B^+ \rightarrow K^+ \mu^+ \mu^-) / \mathcal{B}(B^+ \rightarrow K^+ e^+ e^-)$ (right). It includes a new measurement by the Belle experiment⁸³ using semileptonic tagging of the recoil B (as opposed to fully hadronic reconstruction). Belle finds $R_{D^*} = 0.302 \pm 0.030 \pm 0.011$ with the first uncertainty being statistical and the second systematic. The Standard Model expectation is 0.252 ± 0.003 . Belle also studies additional kinematic distributions that have new physics sensitivity. The Heavy Flavour Averaging Group (HFAG) has computed a new combination of R_{D^*} that includes the latest Belle result, giving⁸⁴ $R_{D^*} = 0.316 \pm 0.016 \pm 0.010$ which is 3.3σ away from the Standard Model value. The two-dimensional combination with R_D increases the significance to 4.0σ .

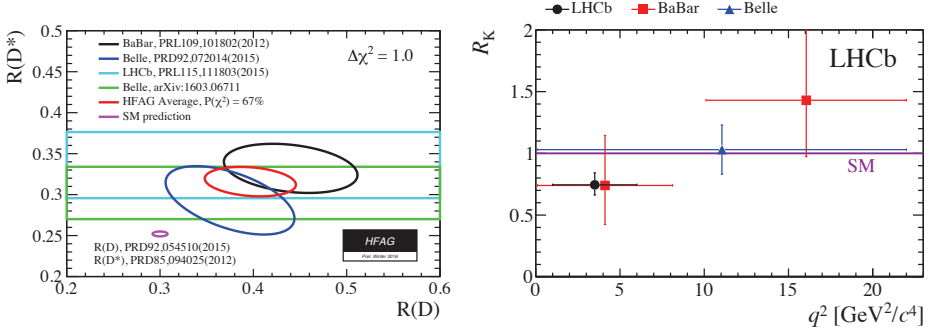


Figure 17 – Ratios of the semileptonic B decays as measured by the B -factory experiments and LHCb. The left panel shows the two-dimensional plane R_{D^*} versus R_D , and the right panel shows R_K versus the invariant mass of the lepton pair. See text for the definitions of the variables.

6.6 Charged lepton flavour violation

A very active field of new physics searches looks for decays that do not conserve the charged lepton flavour. The predictions of such processes within the Standard Model and including massive neutrinos are immeasurably small so that any signal would be a clean sign of new physics. Searches for charged lepton flavour violation have a long history. The canonical channels are $\mu \rightarrow e\gamma$, $3e$, $\mu N \rightarrow eN$ conversion and $\tau \rightarrow \mu\gamma$, 3μ reaching down to branching fractions of order 10^{-13} (10^{-8}) for the former (latter) channels.^g Forthcoming μ -to- e conversion experiments planned in Japan and the US have spectacular perspectives with several orders of magnitude improved sensitivity compared to the current state of the art.

The NA48/2 experiment at CERN has performed a new preliminary analysis⁸⁶ of their 2003–2004 data sample to search for lepton number violation in the decay $K^+ \rightarrow \pi^- \mu^+ \mu^+$. The main background in this channel stems from $K^+ \rightarrow \pi^- \pi^+ \pi^+$ followed by two $\pi^+ \rightarrow \mu^+ \nu$ decays. No excess of events was observed giving the strong limit $\mathcal{B}(K^+ \rightarrow \pi^- \mu^+ \mu^+) < 8.6 \cdot 10^{-11}$ at 90% CL. NA48/2 also studied the dimuon invariant mass spectrum of the opposite-charge $K^+ \rightarrow \pi^+ \mu^+ \mu^-$ data sample for resonances which were not seen. With the new NA62/2 experiment at CERN starting data taking a sensitivity of 10^{-12} for charged-lepton flavour violation in this channel is expected. The search for the decay $\pi^0 \rightarrow e\mu$ is expected to reach a sensitivity of 10^{-11} .

6.7 Rare kaon decays

The NA62 collaboration presented an important preliminary measurement⁸⁷ using their 2007 dataset of the timelike transition-form-factor (TFF) slope a in $F(x) \approx 1 + a \cdot x + \dots$ (c.f. Fig. 18) with $\pi^0 \rightarrow e^+ e^- \gamma$ Dalitz decays (1.2% branching fraction), using about 5 billion triggered π^0 from $K^\pm \rightarrow \pi^\pm \pi^0$ decays and a total of about 20 billion K^\pm in the decay region. The TFF is an input to model the muon $g - 2$ light-by-light scattering contribution.^h A challenge for the $F(X)$ extraction is the proper treatment of the QED radiative corrections that are included in the Monte Carlo (MC) simulation used. A fit using MC-based templates gives $a = (3.70 \pm 0.53 \pm 0.36) \cdot 10^{-2}$, which exceeds in precision previous measurements by factors.

^gThe MEG collaboration just released⁸⁵ their final limit $\mathcal{B}(\mu \rightarrow e\gamma) < 4.2 \cdot 10^{-13}$ at 90% CL, based on the full 2009–2013 dataset (totalling $7.5 \cdot 10^{14}$ stopped muons on target). An upgrade programme MEG II is underway.

^hOther experimental information relevant for that contribution stems from spacelike measurements of the process $e^+ e^- \rightarrow e^+ e^- \gamma^* \gamma^* \rightarrow e^+ e^- \pi^0$ by CELLO, CLEO and BABAR.

The NA62/2 collaboration presented the latest commissioning status⁸⁷ on the way to a first measurement of the ultra-rare decay $K^\pm \rightarrow \pi^\pm \nu \bar{\nu}$. That decay was observed at BNL by the E949 experiment with a measured branching fraction of $(17 \pm 11) \cdot 10^{-11}$ with $(8.4 \pm 1.0) \cdot 10^{-11}$ predicted. The goal by NA62/2 is a branching fraction measurement with 10% precision (assuming Standard Model rate). The experimental requirements are 5 trillion K^\pm decays (giving about 50 signal events) per year, which could already be reached in 2016, and a similar order for the background suppression (dominated by $K^\pm \rightarrow \pi^\pm \pi^0$) to select less than 10 background events per year in the signal regions. The most sensitive discriminating variable is the missing mass $m_{\text{miss}}^2 = (p_{K^\pm} - p_{\pi^\pm})^2$, which is positive and monotonously falling for signal while it can be negative or peaked for backgrounds. The commissioning results showed that the detector performance is close to the design requirements already.

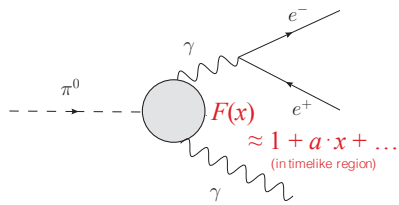


Figure 18 – Feynman graph of the Dalitz decay $\pi^0 \rightarrow e^+e^-\gamma$ used to determine the slope of the timelike transition form factor.

7 Electroweak precision physics

High precision measurements of electroweak observables and the global fit to these were a masterpiece of the LEP era. It led to constraints on the top-quark and Higgs-boson masses before these particles were discovered at, respectively, the Tevatron and the LHC. The direct mass measurements were then found in agreement with the indirect constraints. The discovery of the Higgs boson overconstrains the electroweak fit and dramatically improves its predictability. The fit has thus turned into a powerful test of the Standard Model. The current predictions of the observables most benefiting from the known Higgs boson mass, split into the various uncertainty terms, are⁸⁸: $m_W = 80.3584 \pm 0.0046_{m_t} \pm 0.0030_{\delta_{\text{theo}} m_t} \pm 0.0026_{m_Z} \pm 0.0018_{\Delta\alpha_{\text{had}}} \pm 0.0020_{\alpha_S} \pm 0.0001_{m_H} \pm 0.0040_{\delta_{\text{theo}} m_W}$ GeV, and $\sin^2\theta_{\text{eff}}^l = 0.231488 \pm 0.000024_{m_t} \pm 0.000016_{\delta_{\text{theo}} m_t} \pm 0.000015_{m_Z} \pm 0.000035_{\Delta\alpha_{\text{had}}} \pm 0.000010_{\alpha_S} \pm 0.000001_{m_H} \pm 0.000047_{\delta_{\text{theo}} \sin^2\theta_{\text{eff}}^l}$. Their total uncertainties of 8 MeV and $7 \cdot 10^{-5}$, respectively, undercut the (world average) experimental errors of^{89,90} 15 MeV and $16 \cdot 10^{-5}$, respectively.

The LHC experiments, as do CDF and D0 since long and continuing, are investing efforts into precision measurements of the electroweak observables m_W , m_{top} , and $\sin^2\theta_W^{\text{eff}}$. All are extremely challenging. In this respect, it is worth pointing out that the LHC Run-1 is not over yet. It represents a high-quality, very well understood data sample for precision measurements.

7.1 Top-quark mass

There has been significant progress on the top-quark mass measurements at the LHC achieving similar precision as those performed by the Tevatron experiments. The currently most accurate LHC number is the CMS combination⁹¹ giving $m_{\text{top}} = 172.44 \pm 0.13 \pm 0.47$ GeV, where the first uncertainty is statistical and the second systematic. The most recent Tevatron combination gives⁹² $m_{\text{top}} = 174.34 \pm 0.37 \pm 0.52$ GeV with a tension of 2.4σ or more with the CMS result.

While these kinematic mass measurements provide the best current precision on m_{top} and must be continued, it is also apparent that they approach a difficult systematic uncertainty regime from, mostly, the b -quark fragmentation. A way to improve⁹³ could be to choose more robust observables with respect to the leading systematic effects at the possible price of loosing statistical power. The dilepton kinematic endpoint is an experimentally clean observable, which has however large theoretical uncertainties. More robust could be the selection of charmonium

states⁹⁴ or charmed mesons originating from a b -hadron produced in one of the b -jets. A clean but rare signature. ATLAS and CMS have also invested work into the indirect determination of the top mass from inclusive and differential cross-section measurements. These are promising approaches benefiting from theoretically well defined observables, which are however not yet competitive with the kinematic methods. They also strongly depend on the assumption that no new physics contributes to the measured cross sections. The currently best top pole mass determination from CMS using a precise Run-1 $e\mu$ -based cross-section measurement is⁹⁵ $173.8^{+1.7}_{-1.8}$ GeV in agreement with the direct (kinematic) measurements.

7.2 Weak mixing angle

The CDF, D0,⁹⁹ and LHC experiments^{96,97,98} have extracted the weak mixing angle from Z/γ^* polarisation measurements.^{100,101} The total uncertainty on $\sin^2\theta_W^{\text{eff}}$ at the Tevatron are dominated by statistical effects, that of LHCb has similar statistical and systematic contributions, while for ATLAS and CMS parton density function (PDF) uncertainties are dominant. A data-driven ‘‘PDF replica rejection’’ method applied by CDF allows to reduce the sensitivity to PDF and to update the measurement when improved PDF sets are available. Overall, these are complex measurements (in particular with respect to the physics modelling) that are important to pursue also in view of a better understanding of Z/γ^* production at hadron colliders. The precision obtained is however not yet competitive with that of LEP/SLD.

7.3 W boson mass

ATLAS, CMS and LHCb have presented progress towards a first measurement of the W mass at the LHC using the leptonic W boson decay, which relies on an excellent understanding of the final state.¹⁰² The observables used to probe m_W are the transverse momentum of the lepton ($p_{T,\ell}$), the transverse momentum of the neutrino ($p_{T,\nu}$), measured from the transverse recoil of the event, and the transverse mass of the lepton-neutrino system (m_T). The measurement requires a high-precision momentum and energy scale calibration (including the hadronic recoil) obtained from Z , J/ψ and Υ data, and excellent control of the signal efficiency and background modelling. The biggest challenge is posed by the physics modelling. The production is governed by PDF and initial state interactions (perturbative and non-perturbative), that can be constrained by W^+ , W^- , Z , and $W + c$ data, and the use of NNLO QCD calculations including soft gluon resummation. The experimental m_W probes are very sensitive to the W polarisation (and hence to PDF, including its strange density). Electroweak corrections are sufficiently well known.

The experiments are in a thriving process of addressing the above issues. Many precision measurements (differential Z , $W + X$ cross sections, polarisation analysis, calibration performance, etc.) are produced on the way with benefits for the entire physics programme. Theoretical developments are also mandatory. Altogether this is a long-term effort.

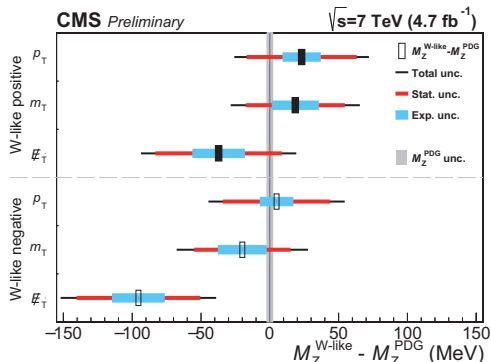


Figure 19 – Difference between the fitted W -like Z mass and the LEP measurement for each m_W probe and W charge.

CMS presented for the first time a m_Z measurement using a W -like $Z \rightarrow \mu^+ \mu^-$ analysis where one muon is replaced by a neutrino that contributes to the missing transverse momentum in the event.^{103,102} It represents a proof-of-principle, although differences with the full m_W analysis remain in the event selection, the background treatment and most of the theory uncertainties, (...). CMS used the 7 TeV dataset to take benefit from the lower number of pileup interactions. The momentum scale and resolution calibration for that measurement relies on J/ψ and Υ data. Track-based missing transverse momentum is used and the W transverse recoil is calibrated using $Z + \text{jets}$ events. The results for the different probes and the positive and negative W -like cases are shown in Fig. 19. Agreement with the LEP measurement is found. The uncertainties, depending on the probe used, are: statistical: 35–46 MeV, total systematic: 28–34 MeV, QED radiation: ~ 23 MeV (dominant), lepton calibration: 12–15 MeV.

8 The LHC at 13 TeV — Standard Model physics

A huge milestone was achieved in 2015 with a record proton–proton collision energy of 13 TeV and high-energy lead–lead collision. After a rocky start, the LHC delivered an integrated proton–proton luminosity of 4.2 fb^{-1} with a peak instantaneous luminosity of $5.2 \cdot 10^{33} \text{ cm}^{-2}\text{s}^{-1}$. The majority of the data were produced with 25 ns bunch crossing distance (as opposed to 50 ns at the beginning of the run). This amount of data already improves the reach for many new physics searches. The year 2015 has also been rewarding for the experiments with many results available for the summer conferences, a huge amount of results released for the CERN end-of-year seminars, and many more at this conference. LHC running in 2016 has already started and is expected¹⁰⁴ to reach up to 25 fb^{-1} integrated luminosity over the year with peak luminosity of about $10^{34} \text{ cm}^{-2}\text{s}^{-1}$.

The integrated luminosity collected by the experiments in 2015 for physics analysis amounts to $3.3\text{--}3.6 \text{ fb}^{-1}$ for ATLAS (depending on the data quality requirements applied), $2.2\text{--}3.3 \text{ fb}^{-1}$ for CMS (0.8 fb^{-1} was taken in a solenoid-off configuration), and 0.32 fb^{-1} for LHCb after luminosity levelling to suppress pileup interactions. The luminosity monitors of the experiments were calibrated with dedicated beam-separation scans to preliminary 5.0% (ATLAS), 2.7% (CMS), 3.8% (LHCb) relative precision. The average number of pileup interactions in ATLAS and CMS were $\langle \mu \rangle_{50 \text{ ns}} \simeq 20$, $\langle \mu \rangle_{25 \text{ ns}} \simeq 13$ (for comparison $\langle \mu \rangle_{8 \text{ TeV}} \simeq 21$), and in LHCb $\langle \mu \rangle_{\text{levelled}} \simeq 1.7$.

8.1 Inclusive W and Z production

Inclusive W and Z boson events represent a rich physics laboratory with strong PDF dependence (the W^+/W^- ratio is sensitive to low- x up and down valence quarks, the W^\pm/Z ratio constrains the strange density), and as probes for QCD and electroweak physics. Their leptonic decays also serve as standard candles to calibrate the electron and muon performance of the detectors.

ATLAS, CMS and LHCb have studied single gauge boson production at 7, 8 and 13 TeV, where LHCb covers a complementary phase space in x, Q^2 owing to its forward acceptance ($2.0 < |\eta| < 4.5$). Initial 13 TeV inclusive Z (W^\pm) cross section measurements were performed by all three experiments (ATLAS and CMS), who find overall agreement with the Standard Model predictions.^{101,105,106,107} Figure 20 shows ratios of cross sections from ATLAS (top panels) and CMS (bottom panels) compared to various PDF sets. Systematic uncertainties cancel to some extent in these ratios so that already a precision of better than 3% is achieved. Similar experiment-versus-theory patterns are observed for both experiments.

Among the Run-1 results presented were measurements of $p_T(Z)$ at 8 TeV from ATLAS¹⁰⁸ (also CMS¹⁰⁹ and LHCb¹¹⁰) showing that soft gluon resummation is needed at low p_T to describe

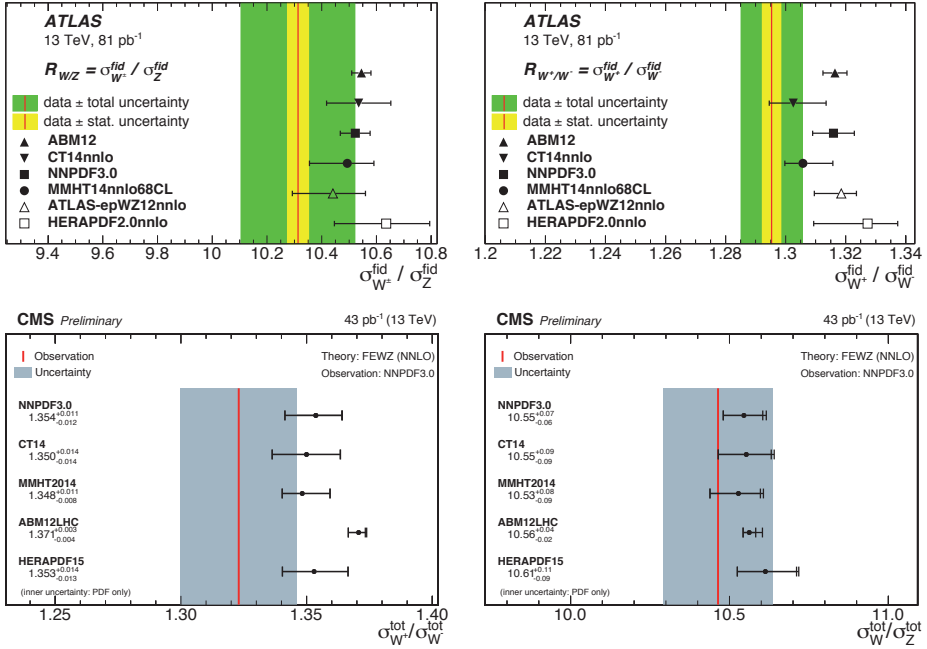


Figure 20 – Ratios of measured fiducial (top, ATLAS) and total (bottom, CMS) cross sections of W^+ to W^- (left) and W^\pm to Z (right) production compared to predictions using various PDF sets.

the data. NNLO calculations lie systematically below the data at high p_T . Charge asymmetry results are found to be well predicted by theory. High-rapidity W and Z cross sections measured by LHCb are well predicted by NNLO theory. A full angular analysis of $Z \rightarrow \mu^+\mu^-$ production and decay at 8 TeV that is sensitive to the Z polarisation and decay structure was performed by CMS.¹¹¹

8.2 Diboson production

Diboson production is an important sector of LHC physics, intimately related to electroweak symmetry breaking. ATLAS and CMS studied diboson production at 7, 8, 13 TeV. Detailed inclusive, fiducial and differential cross-section analyses were performed at 8 TeV, and first 13 TeV results were released.¹¹² Theoretical predictions at NNLO accuracy are needed to match the data.

The ZZ cross section at 13 TeV was measured by ATLAS¹¹³ and CMS,¹¹⁴ WZ by CMS¹¹⁵: all agree with the Standard Model predictions (see Fig. 21 for selected detector-level distributions). The WW cross section at 8 TeV, measured by both experiments,^{116,117} agrees with the NNLO prediction improved by soft p_T resummation. A detailed recent analysis of WZ production at 8 TeV by ATLAS¹¹⁸ shows deviations from the NLO prediction, which is not unexpected. A recent NNLO calculation moves the theory towards the data.¹¹⁹ Measurements of $Z\gamma$ cross sections at 8 TeV by ATLAS¹²⁰ and CMS¹²¹ are matched by NNLO predictions. First evidence for vector-boson scattering (VBS) was reported in 2014 by ATLAS¹²² and by CMS¹²³ in the $W^\pm W^\pm qq$ channel. New 8 TeV VBS searches were released in the $(W/Z)\gamma qq$ (CMS¹²⁴) and $WZqq$ (ATLAS¹¹⁸) modes, not yet leading to an observation of this process. The triboson

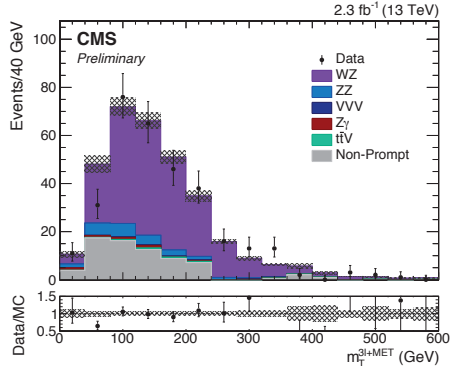
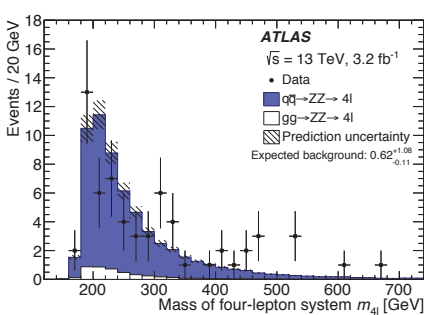


Figure 21 – Detector level distributions of the four-lepton invariant mass (left, ATLAS¹¹³) and the three-lepton plus missing transverse momentum transverse mass (right, CMS¹¹⁵) after corresponding diboson selections.

process $Z\gamma$ was observed by CMS,¹²⁵ evidence for $W\gamma$ was reported by ATLAS¹²⁶ and CMS.¹²⁵ The various diboson analyses provide a large set of anomalous coupling limits.

8.3 Top-quark physics

The cross section of top-antitop quark pair production at 13 TeV is predicted in the Standard Model to increase by a factor of 3.3 over that at 8 TeV. ATLAS and CMS have already studied top production in many ways¹²⁷ at 13 TeV benefiting from a fast analysis turn around in 2015. The robust dilepton $e\mu$ final state provides the most precise inclusive results at all proton-proton centre-of-mass energies. The inclusive $t\bar{t}$ production cross sections as measured by ATLAS, CMS and the Tevatron experiments versus centre-of-mass energy (see Refs.^{128,129} for the 13 TeV results), and compared to theory predictions are shown in the left panel of Fig. 24 Differential cross-section measurements at 13 TeV show reasonable modelling, though some deviations at large jet multiplicity are seen.^{130,131}

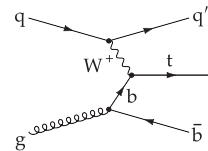


Figure 22 – Feynman diagram for electroweak single top quark production.

ATLAS and CMS have also measured t-channel single top-quark production^{132,133} (see Fig. 22) that is predicted to increase in rate by a factor of 2.5 at 13 TeV over 8 TeV. The cross-section measurements are consistent with this prediction within still sizable experimental uncertainties.¹²⁷ A summary of the measurements and comparison to theory is given in Fig. 24 (right panel).

Of particular interest is the measurement of top-pair production in association with bosons ($t\bar{t}Z$ and $t\bar{t}W$, see Fig. 23 for representative leading order Feynman graphs). These channels are important in their own right (in particular $t\bar{t}Z$, which directly probes the top coupling to the Z boson), but they also represent irreducible backgrounds in $t\bar{t}H$ and many new physics searches. Because of different production processes their respective 13 TeV to 8 TeV cross-section ratios are

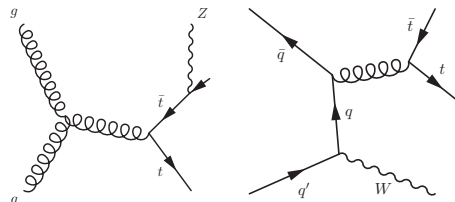


Figure 23 – Feynman diagram for top pair production in association with a Z (left) or a W boson (right).

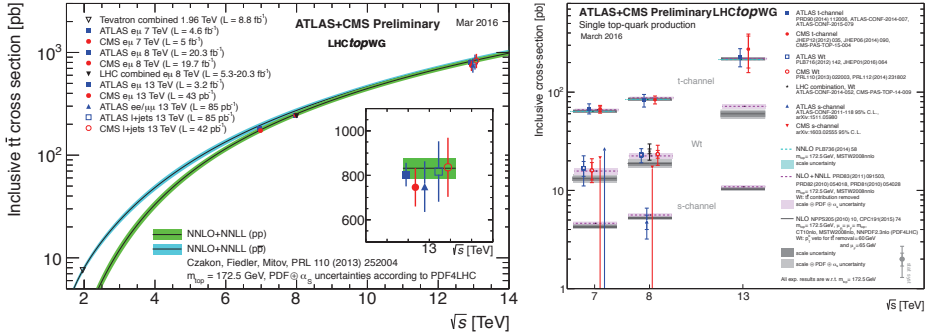


Figure 24 – **Left:** inclusive $pp(\bar{p}\bar{p}) \rightarrow t\bar{t}$ production cross section as measured by ATLAS, CMS and the Tevatron experiments versus centre-of-mass energy. Also shown are the Standard Model predictions at NNLO+NNLL perturbative order. **Right:** single-top production measured by ATLAS and CMS in pp collisions compared to theoretical predictions.

3.6 ($t\bar{t}Z$) and 2.4 ($t\bar{t}W$). ATLAS and CMS showed first 13 TeV results that combine several multilepton final states.^{134,135,136} The most challenging part of the analysis is the estimate of the reducible background due to prompt-lepton misidentification which must be measured in the data. At 8 TeV, both processes were observed and found consistent with the Standard Model predictions (the measured $t\bar{t}W$ cross section was about 1σ high in both ATLAS and CMS). The preliminary results for 13 TeV are: $\sigma(t\bar{t}Z) = 0.92 \pm 0.30 \pm 0.11$ pb, $\sigma(t\bar{t}W) = 1.38 \pm 0.70 \pm 0.33$ pb (ATLAS), and $\sigma(t\bar{t}Z) = 1.07^{+0.35+0.17}_{-0.31-0.14}$ pb (CMS). They agree with the Standard Model predictions computed at NLO, with the $t\bar{t}W$ measurement being again on the high side of the prediction.

The current amount of 13 TeV data is not yet sufficient to probe top decay properties beyond those of the LHC Run-1. Instead, new measurements at 8 TeV and from the Tevatron experiments were presented.^{136,137} The Tevatron top forward-backward asymmetry measurements,^{138,139} $A_{FB}(t\bar{t})$, and its NNLO Standard Model prediction have converged towards each other resolving the previous tension in this observable (see Fig. 25). The measured top charge asymmetries at the LHC are found in agreement with the Standard Model predictions. The D0 experiment has released a new measurement of P and CP -odd observables, where the CP -odd one was found compatible with zero as expected.¹⁴⁰ Top-antitop spin correlations have been established at the LHC and were used by ATLAS to put bounds on “stealth” supersymmetric top partners, so-called top squarks or stop.¹⁴¹ A 4.2σ evidence for spin correlations was presented by D0.¹⁴² Highly suppressed FCNC processes such as $t \rightarrow gq, Zq, Hq$ were probed by ATLAS and CMS with no signal seen.

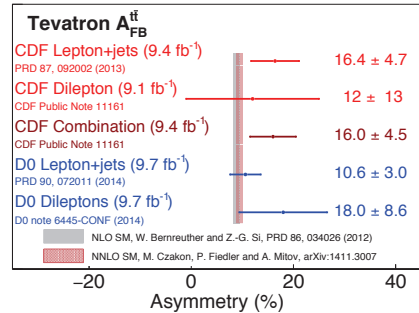


Figure 25 – Summary of $A_{FB}(t\bar{t})$ measurements by CDF and D0 compared to the Standard Model prediction.

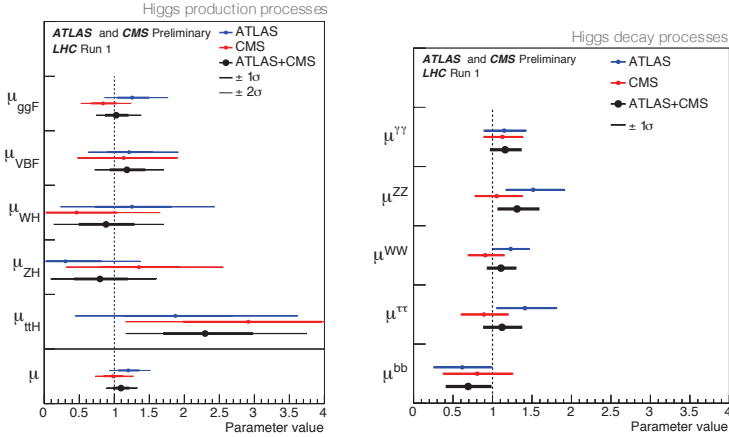


Figure 27 – Higgs boson production signal strengths (left panel) and decay signal strengths (right panel) from the preliminary Run-1 combination of ATLAS and CMS Higgs coupling measurements.¹⁴³ Also shown are the results for each experiment. The error bars indicate the 1σ (thick lines) and 2σ (thin lines on the left panel) intervals. The measurements of the global signal strength μ are also shown.

8.4 Higgs boson physics

In 2015 ATLAS and CMS accomplished a preliminary combination of their Run-1 Higgs boson measurements.^{143,144} Among improved constraints on all couplings it established the observation with more than 5σ significance of the decay $H \rightarrow \tau\tau$ and the Higgs boson production through vector-boson fusion (VBF). The resulting ratios of measured to predicted signal strengths are shown for the production (decay) channels the corresponding decay (production) modes are assumed to be Standard Model like. No significant deviation from one is observed, albeit a somewhat higher than expected ttH cross section is seen. The expected increase in Higgs boson cross section at 13 TeV compared to 8 TeV is between 2 and 2.4 for VH , ggH and VBF, but 3.9 for ttH . A luminosity of 3.3 fb^{-1} at 13 TeV already attains roughly 80% of the Run-1 sensitivity for the latter mode.

Both ATLAS and CMS have finalised their Run-1 searches for lepton flavour violation in Higgs boson decays.^{145,146} While $H \rightarrow \mu e$ is severely bound from other flavour physics measurements, $H \rightarrow \tau\mu, \tau e$ are only weakly constrained. CMS released early 2015 a $H \rightarrow \tau\mu$ result with a slight (2.4σ) excess. ATLAS has completed its full analysis (including a search for $H \rightarrow \tau e$) for

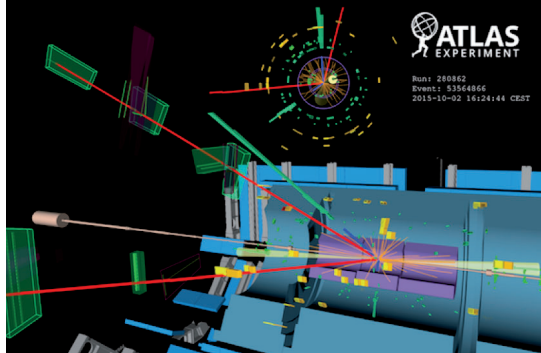


Figure 26 – Display of a $H \rightarrow ee\mu\mu$ candidate from 13 TeV proton–proton collisions measured by ATLAS. The invariant mass of the four lepton system is 129 GeV, the dielectron (dimuon) invariant mass is 91 (29) GeV, the pseudorapidity difference between the two jets is 6.4, the di-jet invariant mass is 2 TeV. This event is consistent with VBF production of a Higgs boson decaying to four leptons.

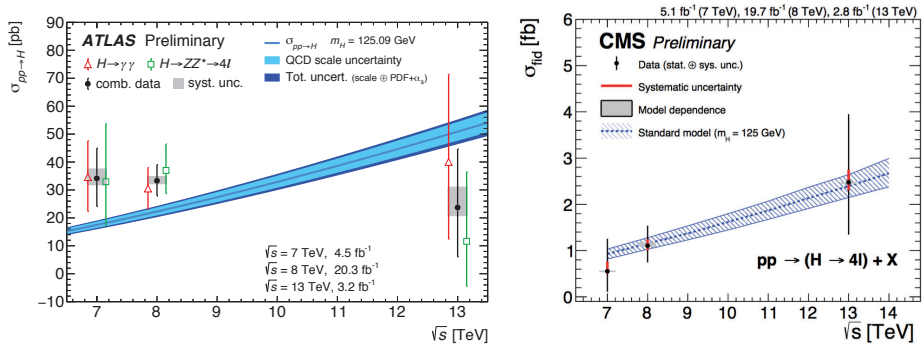


Figure 28 – **Left:** combined inclusive $H \rightarrow 4\ell, \gamma\gamma$ cross sections versus proton–proton CM energy as measured by ATLAS and compared to the NNLO theoretical prediction. **Right:** CMS fiducial $H \rightarrow 4\ell$ cross section versus CM energy.

this conference. The results for $\mathcal{B}(H \rightarrow \tau\mu)$ are $0.53 \pm 0.51\%$ ($< 1.43\%$ at 95% CL) for ATLAS, $0.84^{+0.39}_{-0.37}\%$ ($< 1.51\%$) for CMS, and $\mathcal{B}(H \rightarrow \tau e) = -0.3 \pm 0.6\%$ ($< 1.04\%$) for ATLAS.

Although the sensitivity is yet marginal for inclusive Higgs boson production, ATLAS and CMS have looked in their 13 TeV datasets for $H \rightarrow 4\ell$ and $H \rightarrow \gamma\gamma$ events.^{147,148,149} The observed signal yields are consistent with the theoretical predictions. Figure 28 shows the measured inclusive Higgs boson production cross sections versus the proton–proton centre-of-mass energy for ATLAS (left) and CMS (right).

The CMS collaboration released in record time first 13 TeV results for ttH production searches,^{150,151} which is the only currently accessible channel that directly measures the top–Higgs coupling (c.f. Feynman graph in Fig. 29). All major Higgs boson decay channels, $\gamma\gamma$, multileptons, and bb , were analysed. In particular the latter two channels represent highly complex analyses. The multilepton mode targets Higgs boson decays to $\tau\tau$, $WW \rightarrow 2\ell 2\nu$, and $ZZ \rightarrow 2\ell 2\nu$, 4ℓ together with at least one top-quark decaying leptonically. It requires at least two leptons with the same charge, which greatly reduces Standard Model backgrounds. The dominant remaining backgrounds are misidentified prompt leptons and ttV production. The $H \rightarrow bb$ mode is analysed in the one and two lepton channels. Here, the biggest challenge represents $t\bar{t}$ production associated with heavy flavour quarks (c or b) originating mostly from gluon splitting, which is poorly known and needs to be constrained from data simultaneously with the signal. Figure¹⁵⁰ shows representative plots for the three ttH channels. The results for the relative signal strengths are: $\mu_{ttH(\rightarrow\gamma\gamma)} = 3.8^{+4.5}_{-3.6}$, $\mu_{ttH(\rightarrow\text{leptons})} = 0.6^{+1.4}_{-1.1}$, and $\mu_{ttH(\rightarrow bb)} = -2.0 \pm 1.8$. No significant excess was observed.

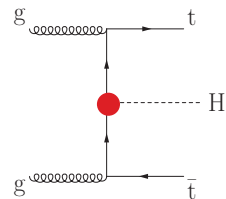


Figure 29 – Feynman diagram for Higgs boson production in association with two top quarks probing the top–Higgs coupling strength.

9 The LHC at 13 TeV — Searches for new physics

Many of the high mass and higher cross section searches for new physics already benefit from the 2015 13 TeV data sample to extend their sensitivity. It represents thus a fresh start after the negative beyond the Standard Model searches from Run-1. The legacy of Run-1 also contained a small number of anomalies that needed to be verified in the Run-2 data. Only 13 TeV searches are discussed in the following.

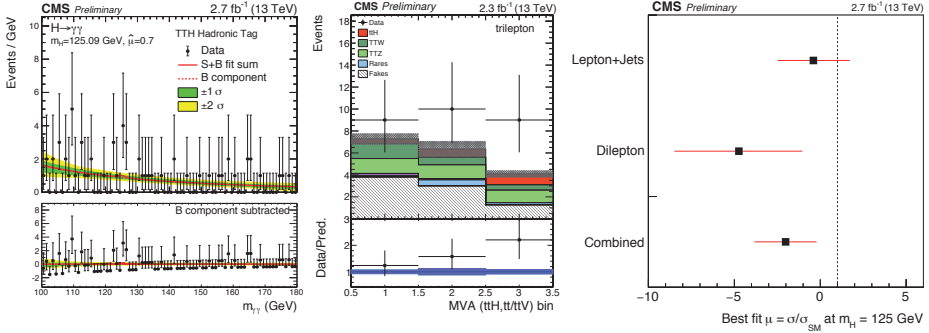


Figure 30 – CMS analyses in the search for ttH production at 13 TeV. The left panel shows the diphoton invariant mass in the hadronic channel with at least 5 jets and on b -tag, the middle panel the BDT output in the triplepton channel of the multilepton search, and the right panel shows the relative signal strengths obtained in the single and dilepton analyses targeting $ttH(\rightarrow bb)$, and their combination.

9.1 Additional Higgs bosons

The observed 125 GeV Higgs boson completes the four degrees of freedom of the Standard Model BEH doublet. Nature may have chosen a more complex scalar sector of, e.g., two BEH doublets, which extends the scalar sector by four more Higgs bosons, of which two are neutral (one CP -even and one CP -odd) and the other two are charged. Both ATLAS and CMS have searched¹⁵² for such additional Higgs bosons in Run-1 and Run-2. For $H \rightarrow \tau\nu$ ($H/A \rightarrow \tau\tau$), the sensitivity of the new data exceeds that of Run-1 for masses larger than 250 GeV (700 GeV). The search for $A \rightarrow Z(\rightarrow \ell\ell, \nu\nu)h_{125}(\rightarrow bb)$ features improved sensitivity beyond about 800 GeV. Searches for $H \rightarrow ZZ(\rightarrow \ell\ell qq, \nu\nu qq, 4\ell)$ and $WW(\rightarrow \ell\nu qq)$ target the > 1 TeV mass range where the bosons are boosted and their hadronic decays are reconstructed with jet substructure techniques. The search for a resonance decaying to $hh_{125}(\rightarrow bb\gamma\gamma)$ had a small excess in Run-1 at about 300 GeV, which could not yet be excluded at 13 TeV. Also performed were searches for resonant and non-resonant $hh_{125}(\rightarrow bb\tau\tau)$ production. None of these many searches exhibited an anomaly so far in the 13 TeV data.

9.2 New phenomena with high-transverse-momentum jets and leptons

Among the first searches performed at any significant increase of collision energy are those for heavy strongly interacting new phenomena.¹⁵³ Figure 31 shows on the left panel the ATLAS dijet invariant mass spectrum^{154,155} and on the right panel the CMS multijet S_T (defined as the scalar sum of the jet transverse momenta) distribution.^{156,157} The measured spectra are compared to phenomenological fits using smoothly falling functions as expected from the QCD continuum. No significant deviation from these fits is seen in the data. The experiments have also looked at dijet angular distributions versus the dijet mass which add further sensitivity to phenomena described by effective contact interactions. An ATLAS analysis¹⁵⁸ looked for new physics in the $\sum p_T$ spectrum of events with at least one high- p_T lepton and jets. ATLAS and CMS have also looked for resonances decaying to heavy-flavour quarks,^{159,160,162} $X \rightarrow b\bar{b}, t\bar{t}$. None of these searches exhibited an anomaly. Second generation scalar lepto-quarkⁱ pair production was searched for by CMS¹⁶¹ in the $(\mu q - \mu q)$ final state excluding such particles below a mass of 1.2 TeV in case of 100% branching fraction to μq .

ⁱLepto-quarks are hypothetical particles carrying both lepton and baryon numbers.

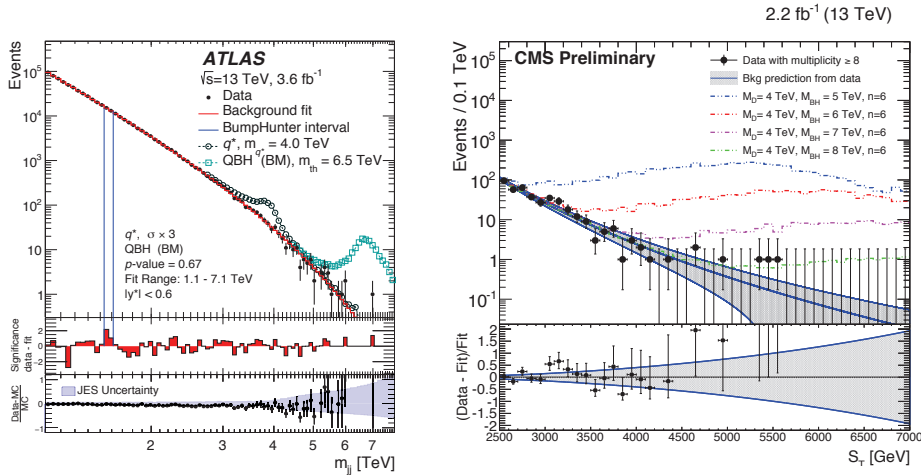


Figure 31 – Dijet invariant mass distribution measured by ATLAS (left) and S_T spectrum in multijet events measured by CMS (right). The data are compared to fits using smoothly falling functions. Also shown are distributions for benchmark signal models.

Important canonical searches involve charged and charged–neutral dilepton pairs.¹⁶³ Excellent high-mass Drell-Yan background modelling is crucial here, which requires to pair detailed differential cross-section measurements with these searches. High- p_T muon reconstruction challenges the detector alignment in particular for the complex ATLAS muon spectrometer structure.¹⁶⁴ Figure 33 shows the ATLAS dielectron mass distribution¹⁶⁵ (left panel) and the CMS¹⁶⁶ transverse mass between the muon and the missing transverse momentum (measuring the neutrino from the transverse balancing of the event, right panel). Figure 32 shows a display of the highest-mass dilepton events measured by CMS in the 2015 data. No anomaly was found. Limits for the traditional sequential Standard Model Z' (W') benchmark are set at 3.4 TeV (4.4 TeV) (for comparison: 2.9 TeV (3.3 TeV) at 8 TeV). ATLAS and CMS also looked into high-mass $e\mu$ (lepton flavour violation) production.^{167,168} The main background here are dilepton top-antitop events. Again, no anomaly was seen.

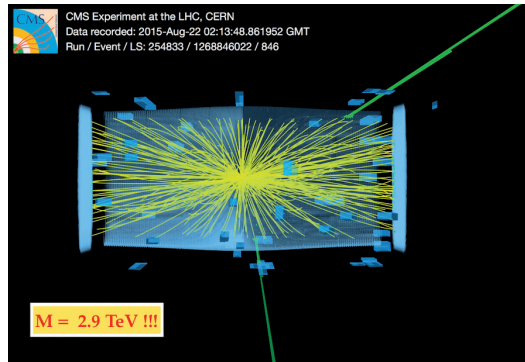


Figure 32 – Display of the highest-mass dilepton pair measured by CMS at 2.9 TeV mass. Each electron candidate has 1.3 TeV E_T , and the two candidates are back-to-back in azimuthal angle. For comparison, the highest-mass Run-1 events found by CMS were at 1.8 TeV (ee), 1.9 TeV ($\mu\mu$).

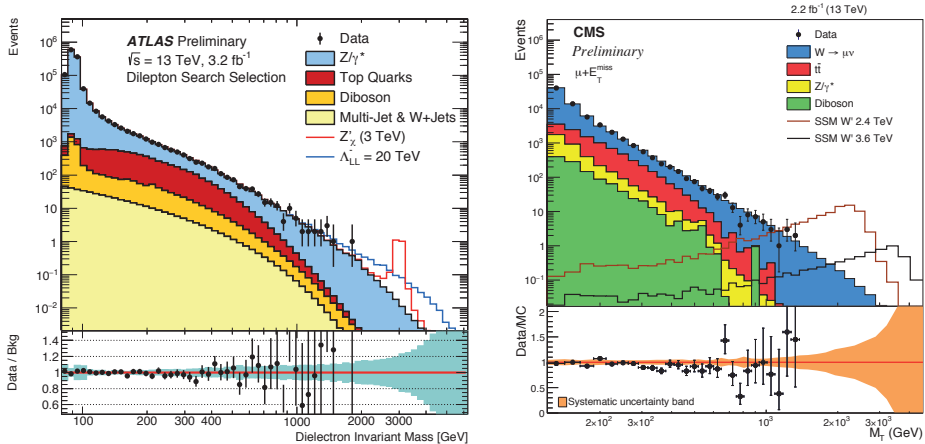


Figure 33 – Dielectron mass distribution measured by ATLAS (left) and the muon–neutrino transverse mass distribution from CMS (right). The data are compared to predictions from (mostly) MC simulation. Also shown are distributions for benchmark signal models.

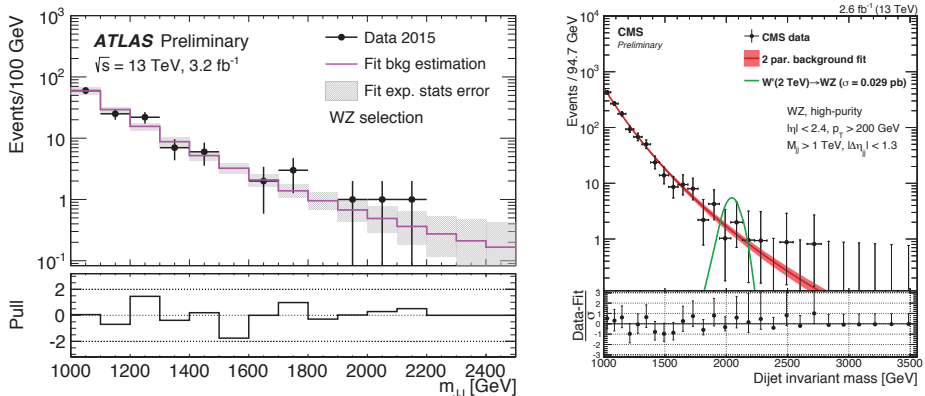


Figure 34 – Dijet invariant mass distributions in the search for a heavy resonance decaying to a W and a Z boson, each of which decays hadronically into a merged jet. The left plot shows ATLAS, the right CMS.

9.3 Diboson resonances (VV , Vh , hh)

Also 13 TeV searches for a diboson resonance were promptly released by ATLAS and CMS.¹⁶⁹ The high p_T of the bosons boosts the hadronic decay products so that jets are merged and analysed using substructure techniques to suppress strong-interaction continuum background. An excess of events was seen at 8 TeV in the fully hadronic $X \rightarrow VV$ ($V = W, Z$) resonance searches^{170,171} around 2 TeV (globally 2.5σ for ATLAS in the WZ mode), which was however not observed in the other weak gauge boson decay channels of similar sensitivity. Figure 34 shows the 13 TeV dijet mass distributions after substructure analysis for ATLAS¹⁷² (left) and CMS¹⁷³ (right). There is no hint of an excess around 2 TeV, but the current statistical precision is not large enough¹⁷⁴ to fully exclude the anomaly seen at 8 TeV. Other diboson resonance searches also do not exhibit discrepancies from the Standard Model expectation.

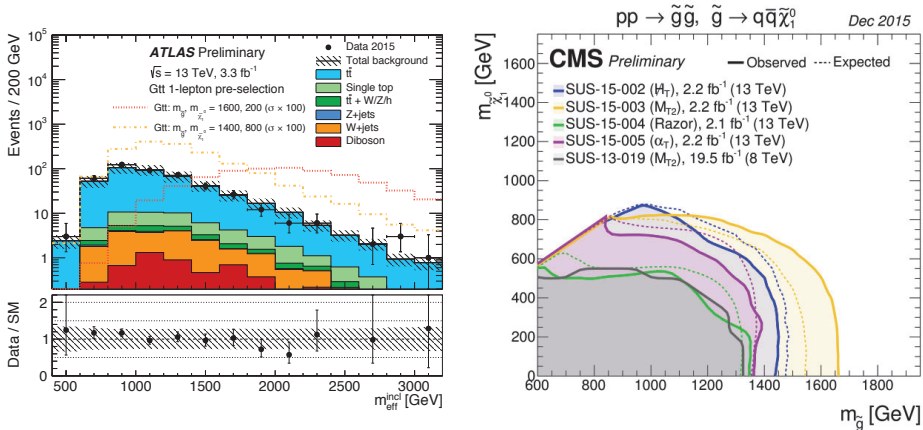


Figure 35 – **Left:** effective mass distribution (scalar sum of selected jet transverse momenta and the event’s missing transverse momentum) measured in the search targeting gluino pair production and decay through intermediate top squarks. Data and Standard Model background estimations are shown together with representative signal benchmark distributions. **Right:** lower limits in the gluino–lightest neutralino mass plane for the four-jet + MET simplified gluino production models used to interpret the jets plus missing transverse momentum searches.

9.4 Supersymmetry

Both ATLAS and CMS have updated their most sensitive searches for high-cross-section strong supersymmetric squark and gluino production using the 13 TeV data sample¹⁷⁵ (c.f. Fig. 36 for representative simplified models). Although the jets plus missing transverse momentum searches benefit from improved background modelling, owing to more accurate MC generators and improved tuning, discrepancies in the extreme phase space regions of these searches remain and are corrected using scale factors determined in data control regions. A total of seven early hadronic 13 TeV analyses were performed by ATLAS and CMS in time of the conference selecting up to ten jets and up to three b -tagged jets.^{176,177} None of these searches observed a significant excess of events in the signal regions. Representative distributions and limits are shown in Fig. 35. In the simplified models used to interpret the searches gluino masses up to 1.7 TeV could be excluded in case of light or moderate-mass neutralinos, exceeding the Run-1 limits by up to 300 GeV.

Inclusive supersymmetry searches also involved events with leptons, where single lepton, dilepton (on and off the Z mass resonance) and same-charge dilepton signatures with additional jets and missing transverse momentum were studied.¹⁷⁸ Such signatures can occur for example when

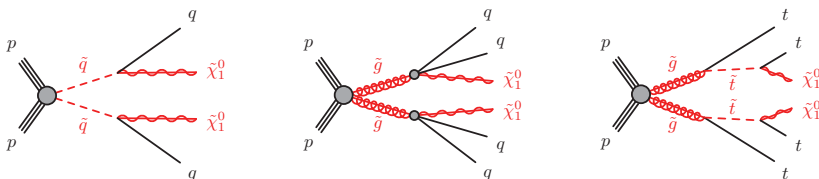


Figure 36 – Simplified models for supersymmetric squark and gluino pair production at the LHC. The right-hand process can occur if the top squark is lighter than the first and second generation squarks as is possible in models with large squark mixing.

gluinos (assumed to be Majorana fermions) decay via intermediate charginos or higher neutralino states or via top squarks. These searches benefit from reduced background levels than in the fully hadronic cases, but often also have lower signal efficiencies due to small leptonic branching fractions. A total of eight searches were presented^{179,180,181,182} with only one (non-significant) anomaly seen. The ATLAS search in $Z \rightarrow \ell\ell$ plus jets plus missing transverse momentum final states¹⁸⁰ exhibits a modest excess of 2.2σ in a signal region that had already shown a 3.0σ excess in the corresponding 8 TeV ATLAS analysis.¹⁸³ Figure 37 shows the observed dilepton mass distribution in data compared to the Standard Model expectation. This excess was not confirmed by CMS at 8 TeV,¹⁸⁴ neither at 13 TeV.¹⁸² A small excess seen by CMS at 8 TeV (2.6σ) in the off- Z dilepton mass region¹⁸⁴ was not confirmed in the 13 TeV data.

Direct production of pairs of third generation bottom and top squarks was also already studied by both ATLAS and CMS.^{185,186,162} The sensitivity of these searches does only moderately exceed that of Run-1 due to the relatively low cross sections of third generation scalar squark production (top-squark pair production has an about six times lower cross section as the corresponding top-quark pair production at equal mass). A total of ten 13 TeV analyses targeted this production and also that of vector-like quark production. Vector-like quarks are hypothetical fermions that transform as triplets under colour and that have left- and right-handed components with same colour and electroweak quantum numbers. For these searches, signatures for pair or single production and decays to bW , tZ and tH were studied.^{187,188} Also considered were exotic $X_{5/3} \rightarrow tW$ particles. No anomaly was seen in these searches.

ATLAS searched for top squark pair production with R -parity violating decays governed by non-zero λ'_{323} couplings to a pair of bs quarks¹⁸⁹ that leads to a four-jet final state with no missing transverse momentum. Employing a hadronic trigger and a data-driven background determination, top squark masses between 250 GeV and 345 GeV were excluded at 95% CL.

The production of long-lived massive particles as it can occur due to large virtuality, low coupling and/or mass degeneracy in a cascade decay, e.g., via the scale-suppressed colour triplet scalar from unnaturalness presented at this conference,¹⁹⁰ is an important part of the LHC search programme.¹⁹¹ ATLAS and CMS presented searches for heavy long-lived supersymmetric particles at 13 TeV using measurements of the specific ionisation loss in the tracking detectors and time-of-flight in the calorimeters and muon systems.^{192,193} Figure 38 shows on the left the distribution of the reconstructed particle mass in CMS compared to the background expectation determined from data together with the distribution of a signal benchmark. The right plot shows limits on the gluino mass versus its lifetime obtained by ATLAS from several analyses covering the full lifetime spectrum.

9.5 Dark matter production

If dark matter particles (assumed to be weakly interacting and massive, WIMPs) interact with quarks and/or gluons they can be directly pair produced in the proton collisions at the LHC.^{194,195} Since the WIMPs remain undetected, to trigger the events a large boost via initial

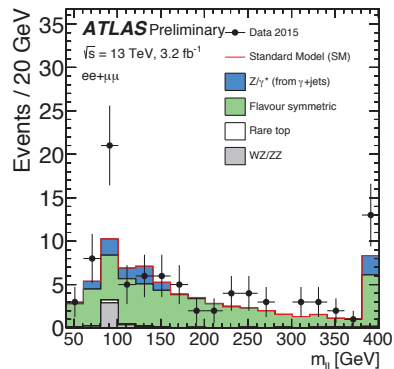


Figure 37 – Dilepton mass distribution observed by ATLAS in a 13 TeV a Z plus jets plus missing transverse momentum search in the dilepton final state compared to the Standard Model expectation.

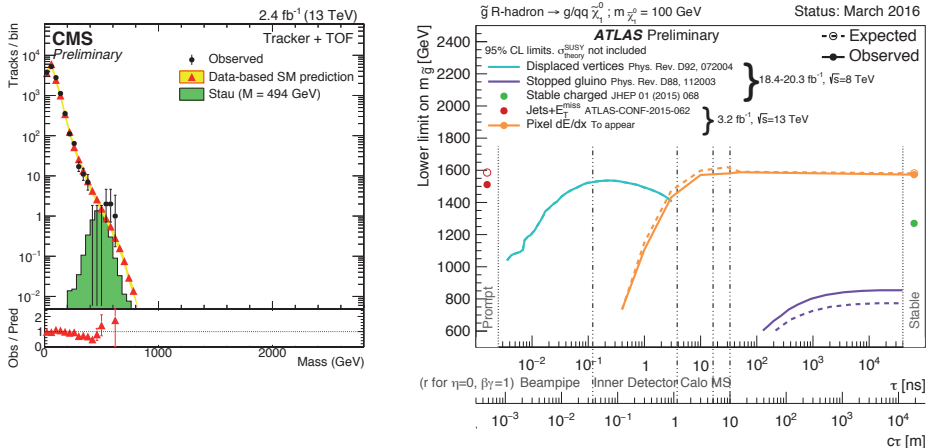


Figure 38 – **Left:** distribution of the reconstructed particle mass in CMS compared to the background expectation determined from data. Also shown is the expected distribution of a long-lived tau slepton signal benchmark. **Right:** limits on the gluino mass versus lifetime obtained by ATLAS. The dots on the left (right) of the plot indicate the limits obtained on promptly decaying (stable) gluinos. Varying searches cover the full lifetime spectrum.

state jet or photon radiation (or other recoiling particles) is needed leading to large missing transverse momentum (MET) from the recoiling WIMP pair. The final state signature depends on the unknown details of the proton–WIMP coupling requiring a large range of “ $X + \text{MET}$ ” searches. The most prominent and among the most sensitive of these is the so-called “mono-jet” search, which extends to a couple of high- p_T jets recoiling against the MET. Large irreducible Standard Model backgrounds in this channel stem from $Z(\rightarrow \nu\nu) + \text{jets}$ and $W(\rightarrow \ell\nu) + \text{jets}$ events, where in the latter case the charged lepton is either undetected or a hadronically decaying tau lepton. These backgrounds are determined in data control regions requiring accurate input from theory to transfer the measured normalisation scale factors to the signal regions. Several 13 TeV results were already released by ATLAS and CMS: jets + MET,^{196,197} photon + MET,¹⁹⁸ $Z/W + \text{MET}$,^{199,200} and $bb/tt + \text{MET}$.²⁰¹ None has so far shown an anomaly.

Figure 39 shows missing transverse momentum distributions measured by ATLAS and CMS in jets + MET and $bb/tt + \text{MET}$ searches, respectively. Figure 40 shows for a specific benchmark model (see figure caption) ATLAS exclusion regions in the DM versus the model’s mediator mass plane as obtained from the jets + MET and photon + MET analyses as well as from the dijet resonance search. These searches have complementary sensitivity.

9.6 Diphoton resonance

Photons have been used at all times in all areas of science as detection probes. A celebrated recent example was the discovery of the Higgs boson via (among other channels) the decay $H \rightarrow \gamma\gamma$. Searches for a new resonance in the diphoton mass spectrum were performed by ATLAS^{203,204} and CMS²⁰⁵ in Run-1 looking for a low to medium mass scalar resonance, or a medium to high mass spin-two resonance motivated by strong gravity models. Diphoton spectra were also analysed in view of high-mass tail anomalies due to new nonresonant phenomena. Searches involving at least three photons were used during Run-1 to look for new physics in Higgs or putative Z' decays.²⁰⁶

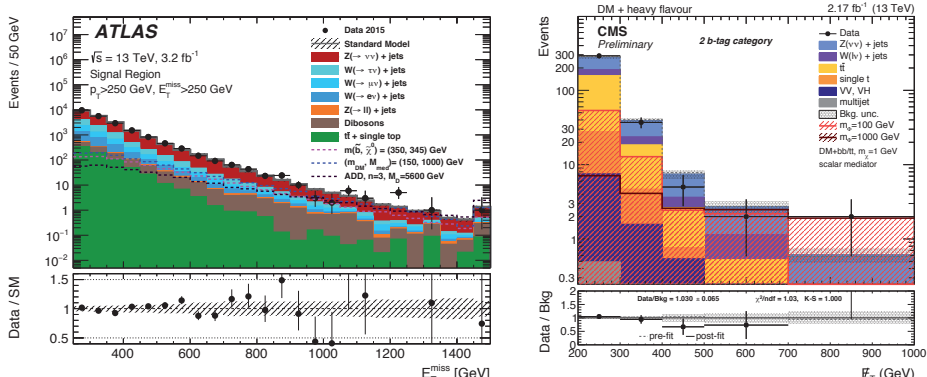


Figure 39 – **Left:** distribution of missing transverse momentum measured by ATLAS at 13 TeV in a “mono-jet” search. The dominant backgrounds stem from leptonic Z and W plus jets events. Also shown are distributions for new physics benchmark models. **Right:** distribution of missing transverse momentum measured by CMS at 13 TeV in a search for heavy-flavour quarks produced in association with large missing transverse momentum.

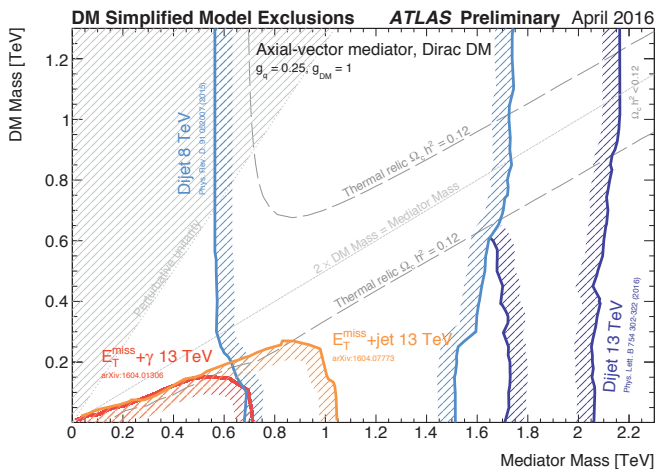


Figure 40 – Regions in a dark matter (DM) mass–mediator mass plane excluded at 95% CL by a selection of ATLAS DM searches, for one possible interaction between the Standard Model and DM, the lepto-phobic axial-vector mediator described in Ref.¹⁹⁵ Dashed curves labelled “thermal relic” indicate combinations of DM and mediator mass that are consistent with the cosmological DM density and a standard thermal history. Between the two curves, annihilation processes described by the simplified model deplete the relic density. A dotted curve indicates the kinematic threshold where the mediator can decay on-shell into DM. Points in the plane where the model is in tension with perturbative unitarity considerations are indicated by the shaded triangle at the upper left. The exclusion regions, relic density contours, and unitarity curve are not applicable to other choices of coupling values or model. See Ref.²⁰² for more information.

Preliminary analyses of the 13 TeV diphoton data presented at the 2015 end-of-year seminars showed enhancements at around 750 GeV invariant diphoton mass in both ATLAS and CMS. This conference featured updated analyses, still preliminary, of the 2015 and for ATLAS also the 8 TeV Run-1 datasets.^{207,208,210,211}

ATLAS²⁰⁷ showed dedicated searches for a spin-zero and a spin-two diphoton resonance. The main difference between these searches are the photon acceptance requirements: for the spin-zero case these are $E_T(\gamma_1) > 0.4 \cdot m_{\gamma\gamma}$, $E_T(\gamma_2) > 0.3 \cdot m_{\gamma\gamma}$, where the indices 1, 2 indicate the leading and subleading photon. In the spin-two case, the fixed requirement $E_T(\gamma_{1/2}) > 55$ GeV is applied. The differences are motivated by the different photon decay angle behaviour in the centre-of-mass of the resonance, resulting in more low- E_T forward photons in the spin-two case. Photons are tightly identified and isolated giving a typical photon purity of about 94%. The background modelling is empirical in the spin-zero analysis, and theoretical in the spin-two case for the dominant irreducible diphoton contribution (the small misreconstructed photon background is determined from data and extrapolated to high mass). This choice is motivated by the high mass reach of the spin-two search.

The top panels of Fig. 41 show the diphoton invariant mass spectra observed with the spin-zero (left) and spin-two (right) selections together with the background estimations. The bottom panels show the local significances obtained when scanning a signal plus background model with varying signal mass and width. The lowest compatibility of the data with the background-only hypothesis is found for the spin-zero case at around 750 GeV and a signal width of about 45 GeV (6% relative to the mass). The p-value of that point is found to correspond to a local significance of $Z = 3.9\sigma$. Taking into account the statistical trials factor inherent in the signal mass and width scan reduces the significance to globally 2.0σ . The corresponding values for the spin-two case are: largest local significance at around 750 GeV and relative width of 7%, local / global significances of $3.6\sigma / 1.8\sigma$. ATLAS compared the event properties in the excess interval (700–800 GeV) with those in the upper and lower sidebands and did not find statistically significant differences. ATLAS also updated its 8 TeV diphoton resonance searches to the latest photon calibration and 13 TeV analysis methods, finding a modest 1.9σ excess at 750 GeV mass and assuming 6% signal width in the spin-zero analysis, and no excess in the spin-two analysis. Assuming the putative resonance to be produced by gluon fusion the production cross section is expected to increase by a factor of 4.7 between 8 TeV and 13 TeV. The compatibility between the observations in the two datasets is then estimated to be at the 1.2σ level for the spin-zero analysis. Would the resonance be produced by light quark–antiquark annihilation, the cross-section scale factor would reduce^j to 2.7 leading to a compatibility at the 2.1σ level between the two datasets. The corresponding numbers for the spin-two analysis and production via gluon fusion / light quark–antiquark annihilation are $2.7\sigma / 3.3\sigma$.

ATLAS also searched for a resonant signal in the $Z\gamma$ final state^{209,152} using leptonic and hadronic Z boson decays and empirical background fits. No significant excess was seen in either spectrum.

CMS²⁰⁸ searched agnostically for a spin-zero or spin-two resonance. The 13 TeV analysis was updated for this conference with a refined electromagnetic calorimeter calibration leading to an about 30% improved mass resolution above $m_{\gamma\gamma} \sim 500$ GeV. CMS also included 0.6 fb^{-1} of solenoid-off data. Photons are selected with $E_T(\gamma_{1/2}) > 75$ GeV and requiring at least one photon to lie in the barrel (absolute pseudorapidity lower than 1.44). The analysis is split into barrel-barrel and barrel-endcap categories that are fit simultaneously. Dedicated energy and efficiency calibrations were developed for the solenoid-off data giving a slightly lower photon identification efficiency and better energy resolution compared to the solenoid-on data. Also the primary vertex finding probability is reduced, which affects the diphoton mass resolution. The

^jAnnihilation of heavy quarks would lead to a larger expected 13 TeV to 8 TeV cross-section ratio of 5.1 for $c\bar{c}$ and 5.4 for $b\bar{b}$.

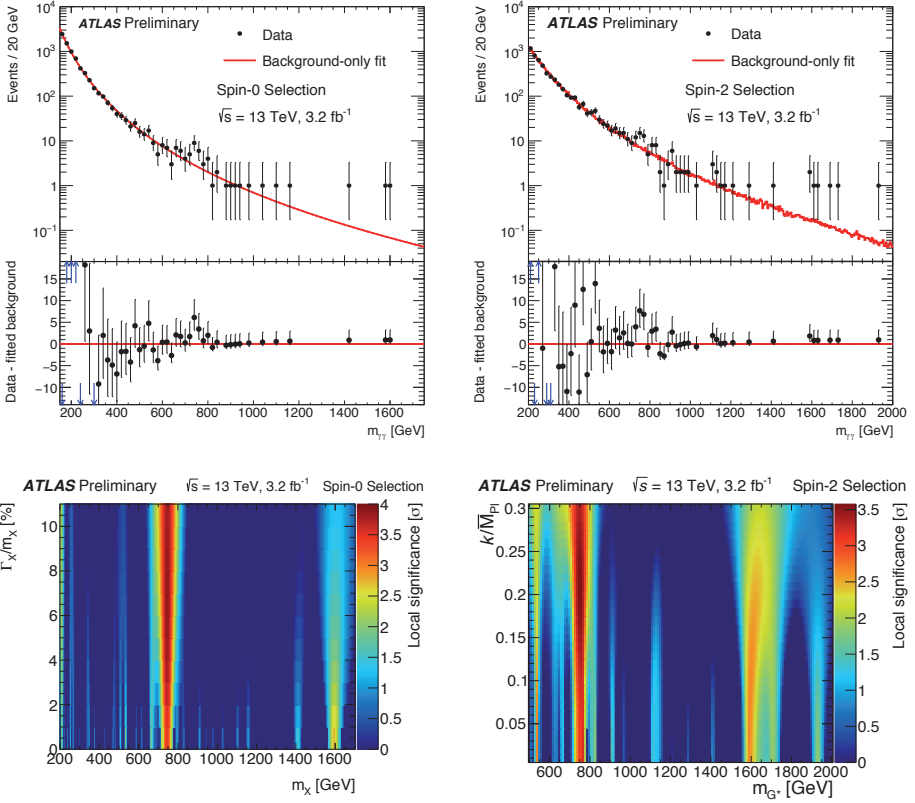


Figure 41 – Top panels: diphoton invariant mass spectra observed with the spin-zero (left) and spin-two (right) selections compared to background estimations. The total numbers of selected events entering the plots are 2878 (5066) for the spin-zero (spin-two) cases. The bottom panels show the local significances obtained when scanning a signal plus background model with varying signal mass and width. Left for the spin-zero and right for the spin-two selections.

backgrounds in all categories are fit using empirical functions.

Figure 42 shows the diphoton invariant mass distributions in the four data categories (barrel/endcap, solenoid-on/off). The resulting p-values versus mass for the narrow-width hypothesis (preferred by the data) are shown in Fig. 43 for the spin-zero (left panel) and spin-two (right panel) cases. In these plots, the red dotted line shows the 13 TeV dataset, the blue dotted line the 8 TeV dataset, and the black solid line their combination computed according to the signal model assumed. The lowest p-values are found at around 750 GeV mass (760 GeV for the 13 TeV data alone). The corresponding local / global significances are $3.4\sigma / 1.6\sigma$, reducing to $2.9\sigma / < 1\sigma$ for the 13 TeV data alone.

The upcoming restart of the LHC is expected to clarify the current uncertainty in the interpretation of these findings.

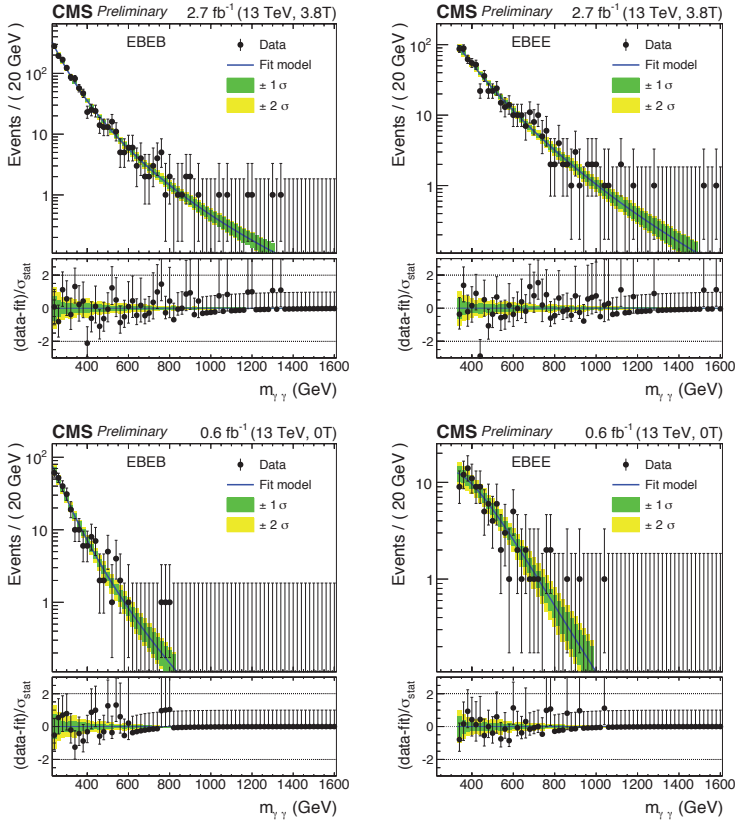


Figure 42 – Diphoton invariant mass distributions measured by CMS in the solenoid-on (top panels) and solenoid-off datasets (bottom panels). The left (right) panels show the barrel-barrel (barrel-endcap) categories. Also shown are the background predictions obtained from the fits to data.

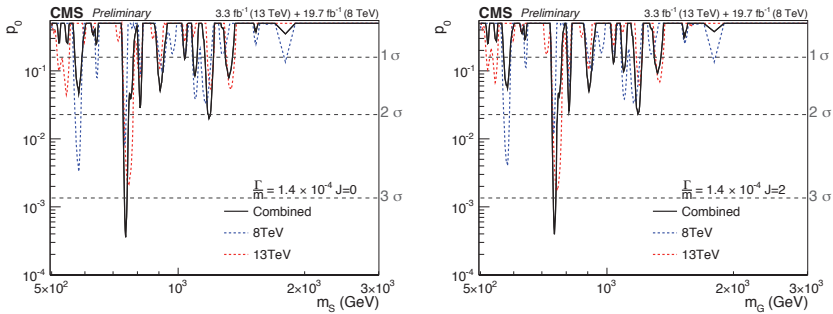


Figure 43 – Local p -value versus mass for a narrow-width signal model as found by CMS for the spin-zero (left) and spin-zero (right) hypotheses. The red (blue) dotted lines give the individual 13 TeV (8 TeV) results and the black solid lines their statistical combinations.

10 Conclusions

The 51st edition of the Moriond Electroweak and Unified Theories conference has been memorable. It exhibited once again the challenges today's experimental physics takes on and overcomes to perform groundbreaking measurements.

The discovery of the Higgs boson required the construction of a huge accelerator and ultra-sophisticated particle detectors to produce Higgs-boson events and find them in several channels buried under 10^{12} times larger backgrounds. The direct observation of gravitational waves required to measure over 4 km length a relative deformation two hundred times smaller than the size of a proton. Similar things can be said about neutrino physics, dark matter searches, etc.

Accomplishing these measurements requires great ideas, visionary leadership, long-term support by governments and society, innovative and highest quality hardware and software, computing resources, operational and maintenance support, precise and unbiased analysis, and above all: dedication.

Given what we have seen this week, I have no worry. We live in an extraordinary period for fundamental experimental research in physics. Congratulations to the 50th anniversary of the conference. There will be ample material for an exciting next half a century!

I thank the organisers for preparing a fascinating conference week and for giving me the opportunity to present the experimental summary.



Contents

1. Introduction	501
2. Neutrino Physics	501
2.1 Results from short-baseline neutrino experiments	502
2.2 Results from long-baseline neutrino experiments	503
2.3 Results from (short-baseline) reactor experiments	505
2.4 Neutrinos from the Sun	507
2.5 Neutrino astronomy	507
2.6 Of which quantum nature are neutrinos?	508
3. Proton decay — GUT messengers	509
4. Direct dark matter searches	510
5. Gravitational waves	512
6. Flavour Physics	514
6.1 Tetraquarks?	514
6.2 CKM Matrix	514
6.3 CP violation and mixing in charm decays	515
6.4 Rare B decays	516
6.5 Flavour anomalies	517
6.6 Charged lepton flavour violation	518
6.7 Rare kaon decays	518
7. Electroweak precision physics	519
7.1 Top-quark mass	519
7.2 Weak mixing angle	520
7.3 W boson mass	520
8. The LHC at 13 TeV — Standard Model physics	521
8.1 Inclusive W and Z production	521
8.2 Diboson production	522
8.3 Top-quark physics	523
8.4 Higgs boson physics	525
9. The LHC at 13 TeV — Searches for new physics	526
9.1 Additional Higgs bosons	527
9.2 New phenomena with high-transverse-momentum jets and leptons	527
9.3 Diboson resonances ($V V$, $V h$, hh)	528
9.4 Supersymmetry	530
9.5 Dark matter production	531
9.6 Diphoton resonance	532
10. Conclusions	537

References

1. The Nobel Prize in Physics, 2015.
2. G. Rossi, these proceedings.
3. S. Lockwitz, these proceedings.
4. LSND Collaboration, Phys. Rev. D 64, 112007 (2001) [hep-ex/0104049].
5. MiniBooNE Collaboration, Phys. Rev. Lett. 110, 161801 (2013) [1303.2588].
6. D. Rutherford, these proceedings.
7. MINERvA Collaboration, Phys. Rev. Lett. 116, 081802 (2016) [1509.05729].
8. A. Timmons, these proceedings.
9. A. Timmons, 1504.04046 (2015).
10. J. Hartnell, these proceedings.
11. NOvA Collaboration, Phys. Rev. D 93, 051104 (2016) [1601.05037].
12. NOvA Collaboration, Phys. Rev. Lett. 116, 151806 (2016) [1601.05022].
13. C. Nielsen, these proceedings.
14. A. Pastore, these proceedings.
15. T2K Collaboration, Phys. Rev. Lett. 116, 181801 (2016) [1512.02495].
16. OPERA Collaboration, Phys. Rev. Lett. 115, 121802 (2015) [1507.01417].
17. Daya Bay Collaboration, Phys. Rev. Lett. 115, 111802 (2015) [1505.03456].
18. Y. Zhang, these proceedings.
19. Daya Bay Collaboration, Phys. Rev. D 93, 072011 (2016) [1603.03549].
20. M. Ishitsuka, these proceedings.
21. Daya Bay Collaboration, Phys. Rev. Lett. 116, 061801 (2016) [1508.04233].
22. A. Hayes, these proceedings.
23. Link to articles about the antineutrino reactor anomaly.
24. N. van Remortel, these proceedings.
25. S. Zavatarelli, these proceedings.
26. Borexino Collaboration, Nature 512, 383 (2014).
27. Borexino Collaboration, J. Phys. Conf. Ser. 675, 012029 (2016).
28. Borexino Collaboration, J. Phys. Conf. Ser. 675, 012025 (2016).
29. J. Auffenberg, these proceedings.
30. IceCube Collaboration, PoS (ICRC2015) 1081 (2015).
31. G. de Wasseige, these proceedings.
32. CUORE Collaboration, Phys. Rev. Lett. 115, 102502 (2015) [1504.02454].
33. P. Gorla, these proceedings.
34. EXO-200 Collaboration, Nature 510, 229 (2014) [1402.6956].
35. EXO-200 Collaboration, Phys. Rev. C 93, 035501 (2016) [1511.04770].
36. Y.-R. Yen, these proceedings.
37. F.T. Avignone, S.R. Elliott, J. Engel, Rev. Mod. Phys. 80, 481 (2008) [0708.1033].
38. V. Takhistov, these proceedings.
39. SuperCDMS Collaboration, Phys. Rev. Lett. 116, 071301 (2016) [1509.02448].
40. E. Lopez Asamar, these proceedings.
41. CRESST Collaboration, Eur. Phys. J. C 76, (2016) [1509.01515].
42. F. Pröbst, these proceedings.
43. XENON100 Collaboration, Phys. Rev. Lett. 109, 181301 (2012).
44. Phys. Rev. Lett. 111, 021301 (2013) no.2.
45. C. Hasterok, these proceedings.
46. XENON100 Collaboration, Phys. Rev. Lett. 109, 181301 (2012) [1207.5988].
47. XENON100 Collaboration, Phys. Rev. Lett. 115, 091302 (2015) [1507.07748].
48. P. Beltrame, these proceedings.
49. LUX Collaboration, Phys. Rev. Lett. 116, 161301 (2016) [1512.03506].
50. LUX Collaboration, Phys. Rev. Lett. 116, 161302 (2016) [1602.03489].
51. A. Rocchi, these proceedings.
52. LIGO/VIRGO Collaboration, Phys. Rev. Lett. 116, 061102 (2016).
53. R.A. Hulse and J.H. Taylor, Astrophys. J. 195, L51 (1975).
54. J.H. Taylor and J.M. Weisberg, Astrophys. J. 253, 908 (1982).
55. Full list of LIGO papers.
56. D0 Collaboration, 1602.07588 (2016).

57. LHCb Collaboration, LHCb-CONF-2016-004 (2016).
58. J. van Tilburg, these proceedings.
59. LHCb Collaboration, Nature Physics 10, 1038 (2015) [1504.01568].
60. LHCb Collaboration, 1604.03475 (2016).
61. LHCb Collaboration, Phys. Rev. Lett. 115, 031601 (2015) [1503.07089].
62. LHCb Collaboration, 1603.04804 (2016).
63. M. John, these proceedings.
64. CKMfitter Group, updates at <http://ckmfitter.in2p3.fr> (2015).
65. LHCb Collaboration, 1602.07224 (2016).
66. A. Pearce, these proceedings.
67. LHCb Collaboration, Phys. Rev. Lett. 108, 111602 (2012);
Erratum Phys. Rev. Lett. 108, 129903 (2012) [1112.0938].
68. LHCb Collaboration, 1602.03160 (2016).
69. LHCb Collaboration, LHCb-CONF-2016-001 (2016).
70. CMS and LHCb Collaborations, Nature 522, 68 (2015) [1411.4413].
71. J. Albrecht, these proceedings.
72. S.K. Swain, these proceedings.
73. C. Bobeth *et al.*, Phys. Rev. Lett. 112, 101801 (2014) [1311.0903].
74. ATLAS Collaboration, 1604.04263 (2016).
75. S. Palestini, these proceedings.
76. LHCb Collaboration, JHEP 02, 104 (2016) [1512.04442].
77. Belle Collaboration, 1604.04042 (2016).
78. L. Hofer, these proceedings.
79. BABAR Collaboration, Phys. Rev. Lett. 109, 101802 (2012) [1205.5442].
80. Belle Collaboration, Phys. Rev. D 92, 072014 (2015) [1507.03233].
81. LHCb Collaboration, Phys. Rev. Lett. 115, 111803 (2015) [1506.08614].
82. P. Goldenzweig, these proceedings.
83. Belle Collaboration, 1603.06711 (2016).
84. Heavy Flavour Averaging Group, $R_{D^{(*)}}$ combination (2016).
85. MEG Collaboration, 1605.05081 (2016).
86. K. Massri, these proceedings.
87. G. Ruggiero, these proceedings.
88. M. Baak *et al.*, Eur. Phys. J. C 74, 3046 (2014) [1407.3792].
89. CDF and D0 Collaborations, Phys. Rev. D 88, 052018 (2013) [1307.7627].
90. ALEPH, DELPHI, L3, OPAL, SLD Collaborations, LEP Electroweak Working Group, SLD Electroweak and Heavy Flavour Groups, Phys. Rept. 427, 257 (2006) [hep-ex/0509008];
ALEPH, DELPHI, L3, OPAL Collaborations, LEP Electroweak Working Group, Phys. Rept. 532, 119 (2013) [1302.3415].
91. CMS Collaboration, Phys. Rev. D 93, 072004 (2016) [1509.04044].
92. CDF and D0 Collaborations, 1407.2682 (2014).
93. B. Stieger, these proceedings.
94. CMS Collaboration, CMS-PAS-TOP-15-014 (2015).
95. CMS Collaboration, 1603.02303 (2016).
96. ATLAS Collaboration, JHEP 09, 049 (2015) [1503.03709].
97. CMS Collaboration, Phys. Rev. D 84, 112002 (2011) [1110.2682].
98. LHCb Collaboration, JHEP 1511, 190 (2015) [1509.07645].
99. A. Bodek, Eur. Phys. J. C, 76, 1 (2016) [1512.08256].
100. A. Bodek, these proceedings.
101. W.J. Barter, these proceedings.
102. M. D'Alfonso, these proceedings.
103. CMS Collaboration, CMS-PAS-SMP-14-007 (2016).
104. J. Wenninger, these proceedings.
105. ATLAS Collaboration, 1603.09222 (2016).
106. CMS Collaboration, CMS-PAS-SMP-15-004 (2016); CMS-PAS-SMP-15-011 (2016).
107. LHCb Collaboration, LHCb-CONF-2016-002 (2016).
108. ATLAS Collaboration, 1512.02192 (2015).
109. CMS Collaboration, 1603.01803 (2016).
110. LHCb Collaboration, JHEP 01, 155 (2016) [1511.08039].

111. CMS Collaboration, Phys. Lett. B 750, 154 (2015) [1504.03512].
112. T. Dai, these proceedings.
113. ATLAS Collaboration, Phys. Rev. Lett. 116, 101801 (2016) [1512.05314].
114. CMS Collaboration, CMS-PAS-SMP-16-001 (2016).
115. CMS Collaboration, CMS-PAS-SMP-16-002 (2016).
116. ATLAS Collaboration, 1604.02997 (2016).
117. CMS Collaboration, 1507.03268 (2015).
118. ATLAS Collaboration, 1603.02151 (2016).
119. M. Grazzini, S. Kallweit, D. Rathlev, M. Wiesemann, 1604.08576 (2016).
120. ATLAS Collaboration, 1604.05232 (2016).
121. CMS Collaboration, JHEP 04, 164 (2015) [1502.05664].
122. ATLAS Collaboration, Phys. Rev. Lett. 113, 141803 (2014) [1405.6241].
123. CMS Collaboration, Phys. Rev. Lett. 114, 051801 (2015) [1410.6315].
124. CMS Collaboration, CMS-PAS-SMP-14-011 (2016).
125. CMS Collaboration, CMS-PAS-SMP-15-008 (2016).
126. ATLAS Collaboration, Phys. Rev. Lett. 115, 031802 (2015) [1503.03243].
127. P. Ferreira da Silva, these proceedings.
128. ATLAS Collaboration, ATLAS-CONF-2016-005 (2016), ATLAS-CONF-2015-049 (2015).
129. CMS Collaboration, CMS-PAS-TOP-16-005; Phys. Rev. Lett. 116, 052002 (2016) [1510.05302].
130. ATLAS Collaboration, ATLAS-CONF-2015-065 (2015).
131. CMS Collaboration, CMS-PAS-TOP-16-008, CMS-PAS-TOP-16-011 (2016).
132. ATLAS Collaboration, ATLAS-CONF-2015-079 (2016).
133. CMS Collaboration, CMS-PAS-TOP-16-003, CMS-PAS-TOP-16-004 (2016).
134. ATLAS Collaboration, ATLAS-CONF-2016-003 (2016).
135. CMS Collaboration, CMS-PAS-TOP-16-009 (2016).
136. E. Monnier, these proceedings.
137. C. Schwabenberger, these proceedings.
138. CDF Collaboration, CDF Public Note 11161 (2015).
139. D0 Collaboration, Phys. Rev. D 90, 072011 (2014) [1405.0421]; D0 note 6445-CONF (2014).
140. D0 Collaboration, D0 Note 6471-CONF (2015).
141. ATLAS Collaboration, Phys. Rev. Lett. 114, 142001 (2015) [1412.4742].
142. D0 Collaboration, 1512.08818 (2015).
143. ATLAS and CMS Collaborations, ATLAS-CONF-2015-044, CMS-PAS-HIG-15-002 (2015).
144. L. Dell'Asta, these proceedings.
145. ATLAS Collaboration, JHEP 11, 211 (2015) [1508.03372]; 1604.07730 (2016).
146. CMS Collaboration, Phys. Lett. B 749, 337 (2015) [1502.07400].
147. ATLAS Collaboration, ATLAS-CONF-2015-059; ATLAS-CONF-2015-060; ATLAS-CONF-2015-069 (2015).
148. CMS Collaboration, CMS-PAS-HIG-15-004; CMS-PAS-HIG-15-005 (2016).
149. S. Zenz, these proceedings.
150. CMS Collaboration, CMS-PAS-HIG-15-008; CMS-PAS-HIG-16-004; CMS-PAS-HIG-15-005 (2016).
151. J.Hauk, these proceedings.
152. A. McCarn, these proceedings.
153. C. Lange, these proceedings.
154. ATLAS Collaboration, Phys. Lett. B 754, 302 (2016) [1512.01530].
155. CMS Collaboration, Phys. Rev. Lett. 116, 071801 (2016) [1512.01224].
156. ATLAS Collaboration, JHEP 03, 026 (2016) [1512.02586].
157. CMS Collaboration, CMS-PAS-EXO-15-007 (2015).
158. ATLAS Collaboration, ATLAS-CONF-2016-006 (2016).
159. ATLAS Collaboration, 1603.08791 (2016); ATLAS-CONF-2016-014 (2016).
160. CMS Collaboration, CMS-PAS-B2G-15-002 (2016).
161. CMS Collaboration, CMS-PAS-EXO-16-007 (2016).
162. P. Everaerts, these proceedings.
163. J. Catmore, these proceedings.
164. ATLAS Collaboration, 1603.05598 (2016).
165. ATLAS Collaboration, ATLAS-CONF-2015-070; ATLAS-CONF-2015-063 (2015).
166. CMS Collaboration, CMS-PAS-EXO-15-005; CMS-PAS-EXO-15-006 (2015).

167. ATLAS Collaboration, ATLAS-CONF-2015-072 (2015).
168. CMS Collaboration, CMS-PAS-EXO-16-001 (2015).
169. M. Bellomo, these proceedings
170. ATLAS Collaboration, JHEP 12, 55 (2015) [1506.00962].
171. CMS Collaboration, JHEP 08, 173 (2014) [1405.1994].
172. ATLAS Collaboration, ATLAS-CONF-2015-073 (2015).
173. CMS Collaboration, CMS-PAS-EXO-15-002 (2015).
174. M. Pierini, these proceedings.
175. C. Young, these proceedings.
176. ATLAS Collaboration, 1602.06194 (2016); 1605.03814 (2016); ATLAS-CONF-2015-067 (2015).
177. CMS Collaboration, 1603.04053; 1602.06581 (2016); CMS-PAS-SUS-15-004; CMS-PAS-SUS-15-005 (2015).
178. H. Kirschenmann, these proceedings.
179. ATLAS Collaboration, 1602.09058 (2016); ATLAS-CONF-2015-067; ATLAS-CONF-2015-076 (2015).
180. ATLAS Collaboration, ATLAS-CONF-2015-082 (2015).
181. CMS Collaboration, CMS-PAS-SUS-15-006; CMS-PAS-SUS-15-007; CMS-PAS-SUS-15-008 (2015/16)
182. CMS Collaboration, CMS-PAS-SUS-15-011 (2015).
183. ATLAS Collaboration, Eur. Phys. J. C 75, 318 (2015) [1503.03290].
184. CMS Collaboration, JHEP 04, 124 (2015) [1502.06031].
185. ATLAS Collaboration, ATLAS-CONF-2015-066 (2015); ATLAS-CONF-2016-007; ATLAS-CONF-2016-009 (2016).
186. CMS Collaboration, CMS-PAS-SUS-16-001; CMS-PAS-SUS-16-002; CMS-PAS-SUS-16-007 (2016).
187. ATLAS Collaboration, ATLAS-CONF-2016-013 (2016).
188. CMS Collaboration, CMS-PAS-B2G-15-006 (2015); CMS-PAS-B2G-15-008; CMS-PAS-B2G-16-002 (2016).
189. ATLAS Collaboration, ATLAS-CONF-2016-022 (2016).
190. T. Gherghetta, these proceedings.
191. Revital Kopeliansky, these proceedings.
192. ATLAS Collaboration, 1604.04520 (2016).
193. CMS Collaboration, CMS-PAS-EXO-15-010 (2015).
194. M. Cremonesi, these proceedings.
195. LHC Dark Matter Forum report, 1507.00966 (2015).
196. ATLAS Collaboration, 1604.07773 (2016).
197. CMS Collaboration, CMS-PAS-EXO-15-005 (2015); CMS-PAS-EXO-16-013 (2016).
198. ATLAS Collaboration, 1604.01306 (2016).
199. ATLAS Collaboration, ATLAS-CONF-2015-080 (2015).
200. CMS Collaboration, CMS-PAS-EXO-16-013 (2016).
201. CMS Collaboration, CMS-PAS-B2G-15-007; CMS-PAS-B2G-15-001 (2016)
202. ATLAS Collaboration, Dark Matter searches summary plot.
203. ATLAS Collaboration, Phys. Rev. D 92, 032004 (2015) [1504.05511].
204. ATLAS Collaboration, Phys. Rev. Lett. 113, 171801 (2014) [1407.6583].
205. CMS Collaboration, Phys. Lett. B 750, 494 (2015) [1506.02301].
206. ATLAS Collaboration, Eur. Phys. J. C 76, 1 (2016) [1509.05051].
207. ATLAS Collaboration, ATLAS-CONF-2016-018 (2016).
208. CMS Collaboration, CMS-PAS-EXO-16-018 (2016).
209. ATLAS Collaboration, ATLAS-CONF-2016-010 (2016).
210. M. Delmastro, these proceedings.
211. P. Musella, these proceedings.

9.
Young Scientists Forum

